

Probing the thermal state of the intergalactic medium at $z > 5$ with the transmission spikes in high-resolution Ly α forest spectra

Prakash Gaikwad¹,^{*} Michael Rauch,²^{*} Martin G. Haehnelt,¹ Ewald Puchwein³,^{*} James S. Bolton⁴, Laura C. Keating⁵, Girish Kulkarni⁶, Vid Iršič,¹ Eduardo Bañados⁷, George D. Becker⁸, Elisa Boera,^{8,9,10,11} Fakhri S. Zahedy², Hsiao-Wen Chen¹², Robert F. Carswell¹³, Jonathan Chardin¹³ and Alberto Rorai¹

¹*Institute of Astronomy and Kavli Institute for Cosmology, Cambridge University, Madingley Road, Cambridge CB30HA, UK*

²*Carnegie Observatories, 813 Santa Barbara Street, Pasadena, CA 91101, USA*

³*Leibniz-Institut für Astrophysik Potsdam (AIP), An der Sternwarte 16, D-14482 Potsdam, Germany*

⁴*School of Physics and Astronomy, University of Nottingham, University Park, Nottingham, NG7 2RD, UK*

⁵*Canadian Institute for Theoretical Astrophysics, 60 St. George Street, University of Toronto, ON M5S 3H8, Canada*

⁶*Department of Theoretical Physics, Tata Institute of Fundamental Research, Homi Bhabha Road, Mumbai 400005, India*

⁷*Max Planck Institut für Astronomie, Königstuhl 17, D-69117, Heidelberg, Germany*

⁸*Department of Physics & Astronomy, University of California, Riverside, CA 92521, USA*

⁹*SISSA, Via Bonomea 265, I-34136 Trieste, Italy*

¹⁰*INAF-Osservatorio Astronomico di Trieste, Via Tiepolo 11, I-34143 Trieste, Italy*

¹¹*IFPU, Institute for Fundamental Physics of the Universe, Via Beirut 2, I-34014 Trieste, Italy*

¹²*Department of Astronomy & Astrophysics, The University of Chicago, Chicago, IL 60637, USA*

¹³*Observatoire Astronomique de Strasbourg, Université de Strasbourg, CNRS UMR 7550, 11 rue de l'Université, F-67000 Strasbourg, France*

Accepted 2020 March 28. Received 2020 March 25; in original form 2020 January 27

ABSTRACT

We compare a sample of five high-resolution, high S/N Ly α forest spectra of bright $6 < z < \sim 6.5$ QSOs aimed at spectrally resolving the last remaining transmission spikes at $z > 5$ with those obtained from mock absorption spectra from the Sherwood and Sherwood–Relics simulation suites of hydrodynamical simulations of the intergalactic medium (IGM). We use a profile-fitting procedure for the inverted transmitted flux, $1 - F$, similar to the widely used Voigt profile fitting of the transmitted flux F at lower redshifts, to characterize the transmission spikes that probe predominately underdense regions of the IGM. We are able to reproduce the width and height distributions of the transmission spikes, both with optically thin simulations of the post-reionization Universe using a homogeneous UV background and full radiative transfer simulations of a late reionization model. We find that the width of the fitted components of the simulated transmission spikes is very sensitive to the instantaneous temperature of the reionized IGM. The internal structures of the spikes are more prominent in low temperature models of the IGM. The width distribution of the observed transmission spikes, which require high spectral resolution ($\leq 8 \text{ km s}^{-1}$) to be resolved, is reproduced for optically thin simulations with a temperature at mean density of $T_0 = (11\,000 \pm 1600, 10\,500 \pm 2100, 12\,000 \pm 2200) \text{ K}$ at $z = (5.4, 5.6, 5.8)$. This is weakly dependent on the slope of the temperature–density relation, which is favoured to be moderately steeper than isothermal. In the inhomogeneous, late reionization, full radiative transfer simulations where islands of neutral hydrogen persist to $z \sim 5.3$, the width distribution of the observed transmission spikes is consistent with the range of T_0 caused by spatial fluctuations in the temperature–density relation.

Key words: methods: numerical - galaxies: intergalactic medium - QSOs: absorption lines - cosmology: large-scale structure of Universe.

* E-mail: pgaikwad@ast.cam.ac.uk (PG); haehnelt@ast.cam.ac.uk (MGH)

© 2020 The Author(s)

Published by Oxford University Press on behalf of the Royal Astronomical Society

1 INTRODUCTION

The reionization of intergalactic H I and He I by ultraviolet photons from stars and black holes in the first galaxies is one of the major phase transitions of the universe (Fan et al. 2001, 2006; Robertson et al. 2010; Bolton et al. 2011; Planck Collaboration et al. 2014, 2018). Photo-heating during the reionization increases the temperature of the intergalactic medium (IGM) (Hui & Gnedin 1997; Trac, Cen & Loeb 2008; McQuinn et al. 2009; McQuinn & Upton Sanderbeck 2016). The thermal and ionization histories of the Universe are thus interlinked and can be used in tandem to understand the process of reionization and the nature of ionizing sources (Haehnelt & Steinmetz 1998; Furlanetto & Oh 2009; McQuinn et al. 2011; Becker et al. 2015; Chardin, Puchwein & Haehnelt 2017; Davies et al. 2018; Keating, Puchwein & Haehnelt 2018; Kulkarni et al. 2019b).

The H I Ly α forest observed along sightlines towards bright QSOs is frequently used to constrain the thermal and ionization state of the IGM at $z < 5$. For underdense or moderately overdense regions, the thermal state of the IGM is often approximated as a power law, parametrized as the temperature at mean density and the slope of the power law (T_0 and γ Lidz et al. 2010; Becker et al. 2011; Garzilli et al. 2012; Rudie, Steidel & Pettini 2012; Boera et al. 2014; Bolton et al. 2014; Hiss et al. 2018; Telikova, Balashev & Shternin 2018; Boera et al. 2019; Telikova, Shternin & Balashev 2019; Walther et al. 2019). Other relevant parameters are the H I photo-ionization rate (Γ_{HI} Rauch et al. 1997; Bolton & Haehnelt 2007; Faucher-Giguère et al. 2008; Calverley et al. 2011; Becker & Bolton 2013; Gaikwad et al. 2017a, b; Viel et al. 2017; Khaire et al. 2019) and the pressure smoothing scale (Gnedin & Hui 1998; Peeples et al. 2010; Kulkarni et al. 2015; Lukić et al. 2015; Rorai et al. 2017a). Due to the rapid increase of the Ly α opacity with redshift, the transmitted Ly α flux at $z > 5$ is close to zero, with the occurrence of a few transmission spikes indicating that the reionization process is inhomogeneous (Becker et al. 2015; Bosman et al. 2018; Eilers, Davies & Hennawi 2018). Analysis of the transmission spikes towards ULAS J1120+0641 QSO ($z_{\text{em}} = 7.084$, Becker et al. 2015; Barnett et al. 2017) with numerical simulations suggests that these spikes correspond to underdense, highly ionized regions of gas (Gnedin, Becker & Fan 2017; Chardin et al. 2018; Kakiichi et al. 2018; Garaldi, Gnedin & Madau 2019; Nasir & D’Aloisio 2019). These studies find that the number and height of the spikes are sensitive to the ionization fraction (x_{HI}) of the IGM, which in turn depends on the photo-ionization rate and the temperature of the gas in the ionized regions. Perhaps somewhat surprisingly, however, Garaldi et al. (2019) found that the spike shape (especially the widths of the spikes) appeared to be only weakly correlated with the temperature of the IGM. We revisit this question here with a larger sample of higher resolution, higher quality Ly α forest spectra, which we compare to high-resolution hydrodynamical simulations of the IGM using the Sherwood and Sherwood–Relics simulation suites. These incorporate simulations with a homogeneous UV background as well as full radiative transfer (RT) simulations of inhomogeneous reionization (Bolton et al. 2017; Kulkarni et al. 2019b, Puchwein et al. in preparation). Note that in the main analysis, we used the Sherwood–Relics simulation suite but complemented these with simulations from the Sherwood simulation suite for additional tests performed in the appendices.

There are several difficulties in probing the effect of the thermal state of the IGM on Ly α transmission spikes. High-redshift QSOs, while intrinsically luminous, are nevertheless faint and observed

spectra are normally taken at moderate resolution as e.g. offered by VLT/X-Shooter, i.e. with 35 km s^{-1} or worse. As a result, most spectra of high-redshift transmission spikes are of rather modest quality and the number of well observed transmission spikes is necessarily still small due to the rarity and faintness of high- z background QSOs (Kulkarni, Worseck & Hennawi 2019a). We improve this situation here and present a sample of five high-resolution (FWHM $\sim 6 \text{ km s}^{-1}$) and high S/N (~ 10) QSO absorption spectra obtained using the Magellan Inamori Kyocera Echelle (MIKE) spectrograph on the Magellan II telescope (Bernstein et al. 2003), and the High-Resolution Echelle Spectrograph (HIRES) on the Keck I telescope (Vogt et al. 1994).

Similarly, simulated transmission spikes may be drawn from simulations with moderate mass or spatial resolution that is sufficient to produce only mock spectra mimicking moderate-resolution spectrographs like X-Shooter (35 km s^{-1} , but see Garaldi et al. 2019). The thermal smoothing scale of the Ly α -transmitted flux due to the IGM temperature ($T \sim 10^4 \text{ K}$, $b \sim 13 \text{ km s}^{-1}$) is, however, significantly smaller than this. As discussed in detail by Bolton & Becker (2009), rather high mass or spatial resolution is required to resolve the small-scale structure in the underdense regions of the IGM probed by Ly α forest spectra at high redshift. Previous theoretical work has focused on analysing the spikes in RT simulations (Gnedin et al. 2017; Chardin et al. 2018; Garaldi et al. 2019). While these simulations are physically well motivated, they are computationally expensive and it is hard to disentangle the effect of the thermal state of the IGM on the transmission spikes from the reionization history and numerical limitations.

We have thus chosen to analyse the transmission spikes first in very high-resolution, high-dynamic range optically thin simulations with different thermal and reionization histories where a single parameter is varied at a time while keeping other parameters fixed. We therefore use simulations from the Sherwood and Sherwood–Relics simulation suite (Bolton et al. 2017, Puchwein et al. in preparation) to show how spike properties depend on the IGM thermal state, the H I photo-ionization rate Γ_{HI} , and (in the appendices) the pressure smoothing scale, as well as the mass resolution and box size of the simulations. Once we have established this, we investigate the effect of inhomogeneous reionization in more physically motivated, spatially inhomogeneous H I reionization simulations including RT (see Keating et al. 2019; Kulkarni et al. 2019b).

Another problem when comparing simulated and observed Ly α forest spectra is the accurate characterization of the transmission spike properties. Transmission spikes are often asymmetric and transmission features appear ‘blended’. The often used simple definition of height and width of spikes based on the maximum and FWHM of the transmitted flux will thus not capture the detailed information contained in the complex spike shapes and could be the reason that the analyses performed so far show little or no correlations with astrophysical parameters (see e.g. the width versus temperature correlation in Garaldi et al. 2019). Characterizing the shape of transmission spikes becomes even more crucial for high S/N, high-resolution QSO absorption spectra. In practice, the problem is very similar to that of the characterization of Ly α absorption lines at lower redshift. To utilize the practical experience gained in this area with existing software packages (e.g. Gaikwad et al. 2017b), we characterize the transmission spikes by fitting Voigt profiles to the ‘inverted’ transmitted flux, $1 - F$. We will later show that the fitted parameters obtained in this way are well correlated with physical properties (e.g. the density and temperature) of the gas associated with the transmission spikes. We will also study how the statistics of the fitted parameters depend on the astrophysical

Table 1. Properties of the QSO spectra analysed in this work (see text for further details).

ID	Name	z_{em}	J	T [h]	(S/N)/pixel	Reference	Instrument	Dates of the observations
1	ATLASJ158.6938-14.4211	6.07	19.27	11.8	7.7	Cehade et al. (2018)	MIKE	2018 March and April
2	PSOJ239.7124-07.4026	6.11	19.37	10.0	6.5	Bañados et al. (2016)	MIKE	2018 March, April, and June
3	ATLASJ025.6821-33.4627	6.34	19.10	6.7	12.0	Carnall et al. (2015)	MIKE	2018 October and December
4	J043947.08+163415.7	6.51	17.47	10.0	30.3	Fan et al. (2019)	MIKE	2018 October and December
5	SDSSJ010013.02+280225.8	6.30	17.60	5.0	20.0	Wu et al. (2015)	HIRES	2017 November

parameters Γ_{HI} , T_0 , and γ . Unlike for absorption lines, there is no direct physical motivation for fitting Voigt profiles to $1 - F$, so this should be considered as a purely heuristic approach to comparing simulated and observed spectra. However, as we will see, this does not mean that the fit parameters obtained do not correlate with physical properties.

The main goal of this paper is to constrain the thermal state of the IGM at $5.3 \leq z \leq 5.9$. The paper is organized as follows: In Section 2, we present the high-resolution spectra of 5 $z > 6$ QSOs and discuss qualitatively the physical origin of Ly α transmission spikes. We present the properties of transmission spikes in optically thin simulations in Section 3 and Section 4. We demonstrate the sensitivity of spike statistics to the IGM thermal state in Section 5. The main results of the paper are presented in Section 5.3 and Section 6 by comparing the observed spike statistics with those from optically thin and RT simulations. We summarize our findings in Section 7. We assume a flat Λ CDM cosmological model (Ω_{Λ} , Ω_{m} , Ω_{b} , σ_8 , n_{s} , h , Y) \equiv (0.692, 0.308, 0.0482, 0.829, 0.961, 0.678, 0.24) consistent with Planck Collaboration et al. (2014) and Planck Collaboration et al. (2018). All distances are given in comoving units unless specified. Γ_{HI} expressed in units of 10^{-12} s^{-1} is denoted by Γ_{12} .

2 TRANSMISSION SPIKES IN HIGH-RESOLUTION, HIGH-REDSHIFT LY α FOREST SPECTRA

2.1 Observations: high-resolution spectra of transmission spikes

The data consist of the high-resolution Echelle spectra of five recently discovered $z > 6$ QSOs. The objects were chosen for their brightness, and individual targets were further selected to maximize the exposure time during a given observing run. Table 1 gives the name of each object, the emission redshift z_{em} , the J AB band magnitude (from the compilation of Ross & Cross 2019), the total on-source exposure time T in hours, and a typical signal-to-noise ratio per pixel. The objects were observed under mostly photometric conditions in sub-arcsec seeing. The first four objects were observed with the MIKE instrument (Bernstein et al. 2003) on the Magellan II telescope at Las Campanas Observatory. A $0.5''$ wide slit gave a measured spectral resolution of 5 km s^{-1} (FWHM). The spectra were binned on to 2 km s^{-1} wide pixels. The spectrum of SDSSJ010013.02+280225.8 was obtained with the HIRES instrument (Vogt et al. 1994) on the Keck I telescope, and a $0.861''$ wide slit, giving a resolution of 6.1 km s^{-1} (FWHM), sampled by 2.5 km s^{-1} wide bins. The data were reduced with a custom pipeline (Becker et al. 2012). Optimal sky-subtraction on the individual, un-rectified exposures was performed according to the prescription by Kelson (2003).

For the continuum model, a power law was assumed. As the high-resolution Echelle spectra had only limited coverage of the unabsorbed region redward of the Ly α emission, the continuum was derived from flux-calibrated, low-resolution spectra of the same QSOs, which extended further to the red. For objects 1–3 (in Table 1), the continua were determined from the discovery spectra, using fits to regions redward of Ly α avoiding broad emission lines, whereas the power law slopes for objects 4 and 5 were taken from the literature cited. The continuum was then scaled uniformly to match the flux-calibrated high-resolution spectrum in the overlap region with the low-resolution spectrum redward of Ly α and divided into the spectrum. To correct for the rapidly variable region of the spectrum near the Ly α emission line, the emission-line region was fitted with a higher order polynomial in the previously continuum divided spectrum, which then was multiplied into the previous continuum fit. The final continuum thus obtained was divided into the data. As we show later, the width of the fitted components of the transmission spikes is relatively robust to continuum fitting uncertainty.

During data reduction, a certain degree of smoothing is introduced into the data that appears as a discrepancy between the RMS fluctuations in the final data and the propagated error array and generally results in an underestimate of the reduced χ^2_{ν} when fitting line profiles. To counteract this problem, a correction factor (generally a number close to unity varying slowly with wavelength) was derived from the observed ratio between the RMS fluctuations and the error array, as determined from wavelength windows in the spectrum with zero flux. A linear fit to the correction factor as a function of wavelength was divided into the error array to obtain a reduced $\chi^2_{\nu} \sim 1$ during profile fitting.

2.2 Characterizing width and height of individual components

Fig. 1 compares transmission spikes in a high-resolution Ly α forest observation of the QSO J043947.08+163415.7 with the MIKE spectrograph with simulated spikes drawn from the Sherwood–Relics simulation suite (see Section 3.1, Puchwein et al. in preparation), for *cold* and *hot* models with a spatially uniform UV background. The transmission spikes have complex shapes composed of many asymmetric and blended features. Even isolated transmission spikes are often highly asymmetric and consist of two or more ‘components’. In order to facilitate a more quantitative discussion of the transmission spikes, we focus on two properties, namely the height and width of individually identifiable components. We quantify these (see Section 4) by fitting the ‘inverted’ transmitted flux, $1 - F$, with multicomponent Voigt profiles, similar to the fitting of Voigt profiles of the transmitted flux, F , often employed at lower redshift to characterize absorption lines.

The best fits to observed and simulated spectra are shown in Fig. 1 by the red curve. The location of individual identified components is marked by black vertical lines. Fig. 1 shows simulated spectra

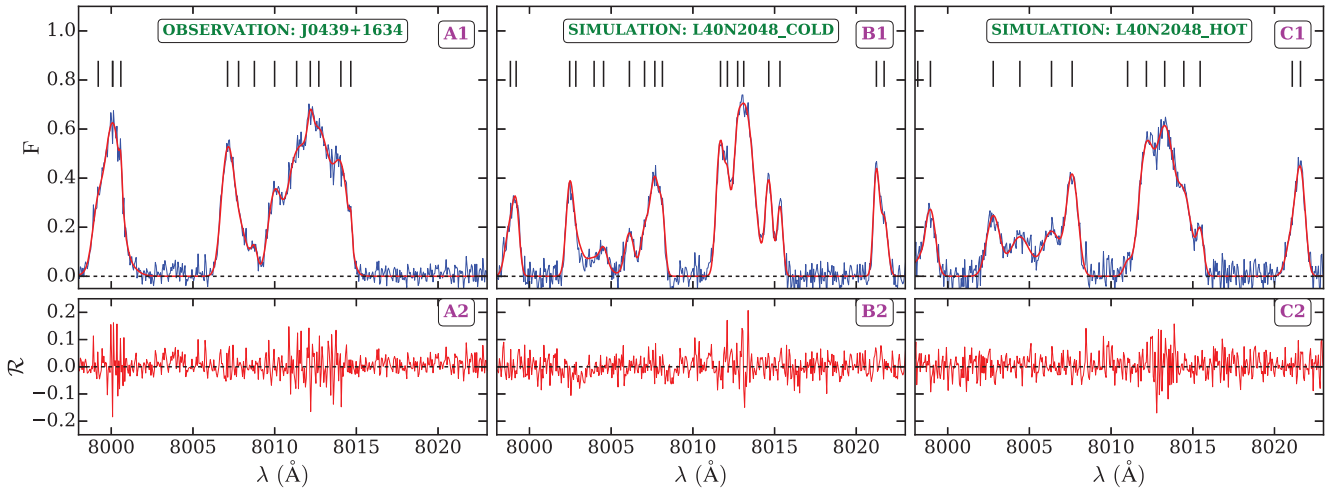


Figure 1. Examples of transmission spikes from observed spectra (panel A1) and simulated spectra from *cold* (panel B1) and *hot* (panel C1) optically thin simulations drawn from the Sherwood–Relics simulation suite at $z \sim 5.59$. The widths and heights of the spikes are sensitive to the thermal and ionization state of the IGM. The shape and number of spikes in the observed spectra are similar to the simulated spectra from the *hot* model. The resolution and noise properties of the simulated spectra are chosen to match the observed spectra. As described in the main text, we fit the ‘inverted’ transmitted flux, $1 - F$, with multicomponent Voigt profiles using the software package VIPER described in detail in Gaikwad et al. (2017b). In VIPER, the number of components to be fitted in given region is decided automatically by minimizing the Akaike information criteria with correction (see Gaikwad et al. 2017b, for details). The top panels show the input spectra (F , blue solid curve) and the fitted spectra (F , in red solid curve). The black solid lines mark the location of the centres of Voigt components identified and fitted by VIPER. The bottom panels show that the residuals between the input and fitted spectra are random and less than 11 per cent. The number of components identified in the *cold* model is larger than in the *hot* model due to the smoother transmitted flux distribution.

for the *hot* and *cold* models and illustrates the sensitivity of spike features to the thermal state of the IGM. The main effect of increase in IGM temperature is to reduce the internal structure of the spikes (i.e. more blending). As a result, fewer and broader components are required to fit the transmission spikes in the *hot* model. In general, the spikes in the *hot* model are (i) broader, (ii) larger in height, (iii) more asymmetric, and (iv) more blended (hence fewer in number) than those in the corresponding *cold* model. It is interesting to note that the number and shape of the spikes in the *hot* model are qualitatively very similar to those in the observed spectra. We will analyse this more quantitatively below.

2.3 The origins of transmission spikes

The complex shapes of the transmission spikes shown in the last section will be a superposition of features in the line-of-sight distribution of density, temperature, photo-ionization rate, and peculiar velocity. To get a better feel for this in Fig. 2, we show mock spectra where we isolate the effect of varying these parameters, one at a time. Fig. 2 illustrates how the variation in any of these physical quantities along a sightline can lead to regions of smaller H I optical depth and hence transmission spikes. Panels A1–A6, B1–B6, and C1–C6 show the effect of underdensity, enhanced Γ_{HI} , and enhanced temperature along a sightline, respectively. All these effects can result in a smaller number density of neutral hydrogen, n_{HI} , along the sightline. Panels D1–D6 show that a diverging peculiar velocity field along the sightline can also produce transmission spikes. Hot, ionized underdense regions subjected to high photo-ionization rates and diverging peculiar velocities will thus produce the most prominent transmission spikes in high- z QSO absorption spectra (Gnedin et al. 2017; Chardin et al. 2018; Garaldi et al. 2019). The transmission spikes shown in Fig. 2 are by construction isolated, symmetric, and simple. As discussed in the previous section, transmission spikes in both observed spectra

and spectra drawn from cosmological hydrodynamical simulations have complicated shapes, as generally more than one of the above effects contribute.

3 TRANSMISSION SPIKES IN OPTICALLY THIN SIMULATIONS

3.1 The Sherwood and Sherwood–Relics simulation suites

We use cosmological hydrodynamical simulations from the Sherwood–Relics simulation suite to investigate transmission spikes in the high-redshift Ly α forest; see Table 2 for an overview. The simulations were performed with a modified version of the P-GADGET-3 code (itself an updated version of the GADGET-2 code presented in Springel 2005). The code uses a tree-particle mesh gravity solver for following cosmic structure formation and a manifestly energy and entropy-conserving smoothed particle hydrodynamics scheme (Springel & Hernquist 2002) for following the hydrodynamics. The Sherwood–Relics simulations build upon the original Sherwood simulation suite (which is used in Appendix C to study numerical convergence) in that the initial conditions were generated in the same way, and much of the modeling of the IGM and Ly α forest is based on similar methods (Bolton et al. 2017).¹

Our main production runs follow 2×2048^3 particles in a $(40 h^{-1} \text{ cMpc})^3$ volume, corresponding to a gas mass resolution of $9.97 \times 10^4 h^{-1} M_{\odot}$. For the gravitational softening, we adopt $0.78 h^{-1} \text{ ckpc}$. Star formation is treated with a rather simplistic but numerically efficient scheme in which all gas particles with densities larger than 1000 times the mean cosmic baryon density and temperatures smaller than 10^5 K are converted to collisionless star particles. While this does not produce realistic galaxies, it allows robust predictions of the properties of the IGM (Viel, Haehnelt &

¹<https://www.nottingham.ac.uk/astronomy/sherwood/>

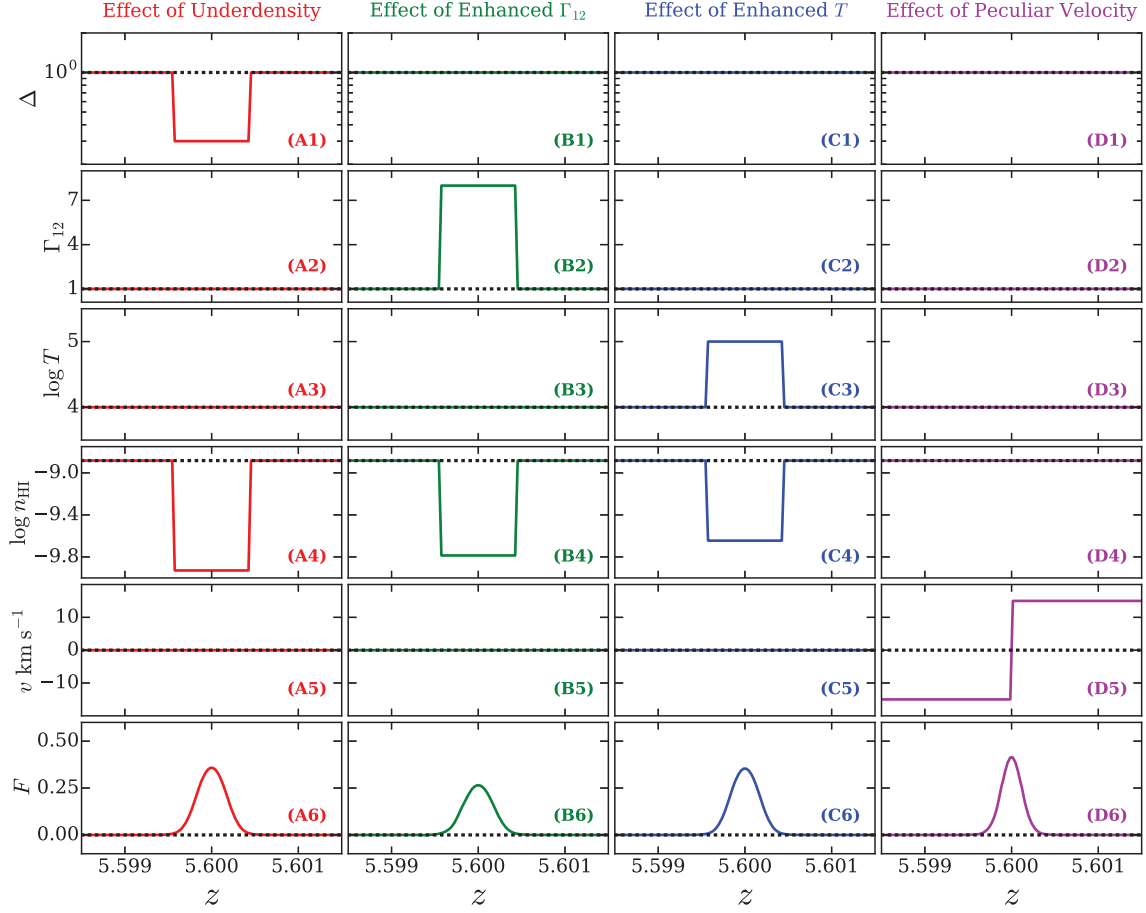


Figure 2. Illustration of the origin of transmission spikes due to the variation of individual physical parameters. Each row displays the variations in line of sight density (Δ), HI photo-ionization rate (Γ_{12}), temperature (T), HI number density (n_{HI}), peculiar velocity (v), and transmitted Ly α flux, F . The black dashed lines show the default values. In each column, a different physical parameter is varied. In the first three columns (i.e. for varying Δ , Γ_{12} and T), the occurrence of spikes is due to a change in n_{HI} . Panels D1–D6 instead show the formation of a transmission spike due to a diverging velocity flow along the sightline while n_{HI} remains constant. Realistic transmission spikes (see Fig. 4) have more complicated shapes and will be due to a combination of these effects.

Table 2. Origin of transmission spikes due to variation in physical parameters in our simulations at $5.5 < z < 5.7$ (as shown in Fig. 2).

Simulation	Underdensity ^a	Fraction of spikes (in per cent) showing the effect of		
		Enhanced Γ_{HI} ^b	Enhanced T ^c	Peculiar velocity ^d
L40N2048_DEFAULT ^e	89.1	—	5.7	18.8
L40N2048_COLD ^e	89.3	—	4.9	14.8
L40N2048_HOT ^e	89.8	—	5.5	19.9
L40N2048_ATON	84.4	56.8	50.1	19.5
L40N2048_PATCHY	79.2	54.7	40.3	18.4

Notes. ^aFraction of all spikes with $\Delta_{\tau} \leq 1$.

^bFraction of all spikes with $\Gamma_{\text{HI}} \geq \Gamma_{\text{HI, median}}$ where $\Gamma_{\text{HI, median}}$ is the optical depth weighted median Γ_{HI} calculated from all the sightlines (i.e. regions with and without spikes). ^cFraction of all spikes with $T_{\tau} \geq T_{\tau, \text{median}}$

where $T_{\tau, \text{median}}$ is the optical depth weighted median temperature calculated from all the sightlines (i.e. regions with and without spikes). ^dFraction of all spikes with $\Delta v \geq 6 \text{ km s}^{-1}$ where Δv is difference between mean velocity on redward and blueward side of spike centre. For diverging velocity flow $\Delta v > 0$, whereas for converging velocity flow $\Delta v < 0$. The limit of $\Delta v = 6 \text{ km s}^{-1}$ corresponds to the spectral resolution of the instrument.

^e L40N2048_DEFAULT L40N2048_COLD and L40N2048_HOT are optically thin simulations that do not include fluctuations in Γ_{HI} .

Springel 2004a). Photo-heating and photo-ionization are followed based on external UV background models. In a departure from the Sherwood simulations, we use a non-equilibrium ionization and cooling/heating solver (Puchwein et al. 2015; Gaikwad et al. 2019) for following the thermochemistry of hydrogen and helium. This ensures that no artificial delay between the reionization of gas and its

photo-heating is present. We have also replaced the slightly modified Haardt & Madau (2012) UV background used in Sherwood with the *fiducial* UV background model from Puchwein et al. (2019) in our *default* run. This results in a more realistic reionization history with hydrogen reionization finishing at $z \approx 6.2$. The *cold/hot* models were obtained by decreasing/increasing the HI and HeI

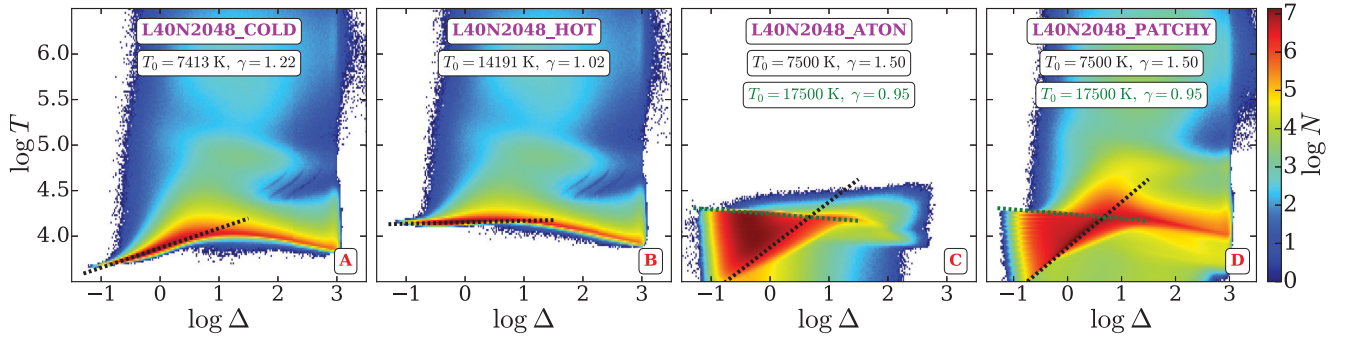


Figure 3. Comparison of the temperature-density relation (TDR) in the *cold* (panel A), *hot* (panel B), *aton* (panel C), and (panel D) simulations at $z = 5.8$. The *cold* and *hot* models correspond to the optically thin Sherwood–Relics simulations. The *aton* simulation is post-processed with the RT code ATON, while the *patchy* simulation includes the effect of pressure/Jeans smoothing as well as the shock heating of the gas. For optically thin simulations, the TDR in underdense and moderately overdense regions can be approximated as a power-law relation ($T = T_0 \Delta^\gamma$) at $\Delta \leq 10$. The best-fitting relation in the *cold* and *hot* models is shown by the black dashed lines. By construction, the temperature of the gas with $\Delta \leq 10$ in the *hot* model is consistently larger than that in the *cold* model. As a result, the heights and widths of the components to be fitted to the transmission features are expected to be different in the *hot* and *cold* models. Unlike the optically thin simulations, the RT simulations (*aton* and *patchy*) do not exhibit a single power-law TDR at $\Delta \leq 10$. For visual purposes, we show two power laws that cover the range in temperature for the RT runs (panel C and D). The absence of gas with $T > 30\,000$ K in *aton* is because the shock heating is not captured self-consistently in the *aton* runs. We plot mass weighted (SPH particle) temperature and density in panels A, B, and D, while we plot volume-weighted temperature and density (calculated on grids) for the *aton* model (panel C). As a result, the number of gas elements (at $\Delta \leq 10$) between the two straight power-law TDR lines is larger in the *aton* simulations than in the *patchy* simulations. Note that gas with $\Delta > 10^3$ and $T < 10^5$ K has been converted into stars in all these simulations (Viel et al. 2004a). We discuss the TDR for optically thin and RT simulations in Section 3.2 and Section 6.2, respectively.

photo-heating rates in the *fiducial* UV background model by a factor of 2 and the He II photo-heating rate by a factor of 1.7, while keeping all photo-ionization rates fixed. Mock Ly α forest spectra were extracted from all simulations as described in Bolton et al. (2017) (see also Gaikwad et al. 2018, 2019). Throughout this work, we use simulations from the Sherwood–Relics simulation suite for the main analysis. Additional simulations from the Sherwood simulation suite are used for convergence tests as described in Appendix C.

3.2 The temperature density relation (TDR) in optically thin simulations

Fig. 3 shows the TDR in the *hot* and *cold* models of the Sherwood–Relics simulation suite. We shall compare the *hot* and *cold* models to study the effect of temperature on transmission spikes. Note that the *hot* model is not only hotter than the *cold* and the *default* models but also has a flatter temperature density relation, and that the ionization state of the gas is also different in the models. This is because the recombination coefficient is temperature-dependent. For the same photo-ionization rate, the HI fraction is therefore smaller in the *hot* model. The models *aton* and *patchy* incorporate the effect of inhomogeneous UV background that we describe in Section 6.

3.3 Examples of transmission spikes in the hot and cold optically thin simulations

Fig. 4 shows the relevant physical properties along the two sightlines in the *hot* and *cold* models. As expected, the *hot* model shows (i) a smoother density (Δ) field in real space, (ii) a smaller HI fraction (x_{HI}), (iii) a larger temperature (T), and (iv) a smoother velocity (v) field compared to the corresponding *cold* model. The smoothing of the real-space density field and the velocity field can be attributed to the increased effect of pressure smoothing in the *hot* model. The resultant Ly α optical depth and transmitted flux calculated from the Δ , x_{HI} , T , and v fields are shown in panels A6–B6 and panels A7–B7, respectively. Note that the location of spikes in the green-

and yellow-shaded regions in redshift space differs in real space due to the effect of peculiar velocities. The transmission spikes in the *hot* and *cold* models have complicated shapes, qualitatively similar to that in the observed spectra (Fig. 1). The smoother transmission features in the simulated spectra of the *hot* model are more similar to those in the observed spectra than those in the more ‘spiky’ spectra in the *cold* model.

In both models, the transmission spikes correspond to regions of low HI optical depth ($\tau_{\text{HI}} \leq 4$, black dashed line). The peaks in transmission are well correlated with those in the optical depth weighted overdensities ($\Delta_\tau < 0.8$).² It is clear from Fig. 4 that the spikes in the *hot* model are smoother, broader, and more prominent than in the *cold* model. Furthermore, the number of individual transmission components is significantly smaller in the *hot* model than in the *cold* model due to the ‘thermal blending’ of transmission features. The shape and number of transmission spikes in our simulated spectra are clearly sensitive to the thermal and ionization states of the IGM in a manner that we will quantitatively discuss below.

Table 2 shows the physical effects responsible for the occurrence of transmission spikes in the optically thin *hot* and *cold* simulations. Most of the spikes (~ 89 per cent) in the *hot* and *cold* models occur in underdense regions. Around 15 per cent of spikes show a diverging velocity field along the sightline. The effect of enhanced temperature on the occurrence of transmission spikes is marginal in both *hot* and *cold* optically thin simulations.

In summary, Fig. 4 and Table 2 show that underdense ($\Delta_\tau < 0.8$), more highly ionized (minimum in x_{HI}) and hotter regions along a sightline produce more prominent spikes. This motivates us to quantify the shape of spikes and to introduce statistics that are sensitive to the thermal and ionization parameters of the IGM.

² Δ_τ accounts for the redshift space effect of peculiar velocity on Δ . To assign a single overdensity/temperature to each transmission spike, we calculate flux weighted overdensity/temperature (also see Garaldi et al. 2019).

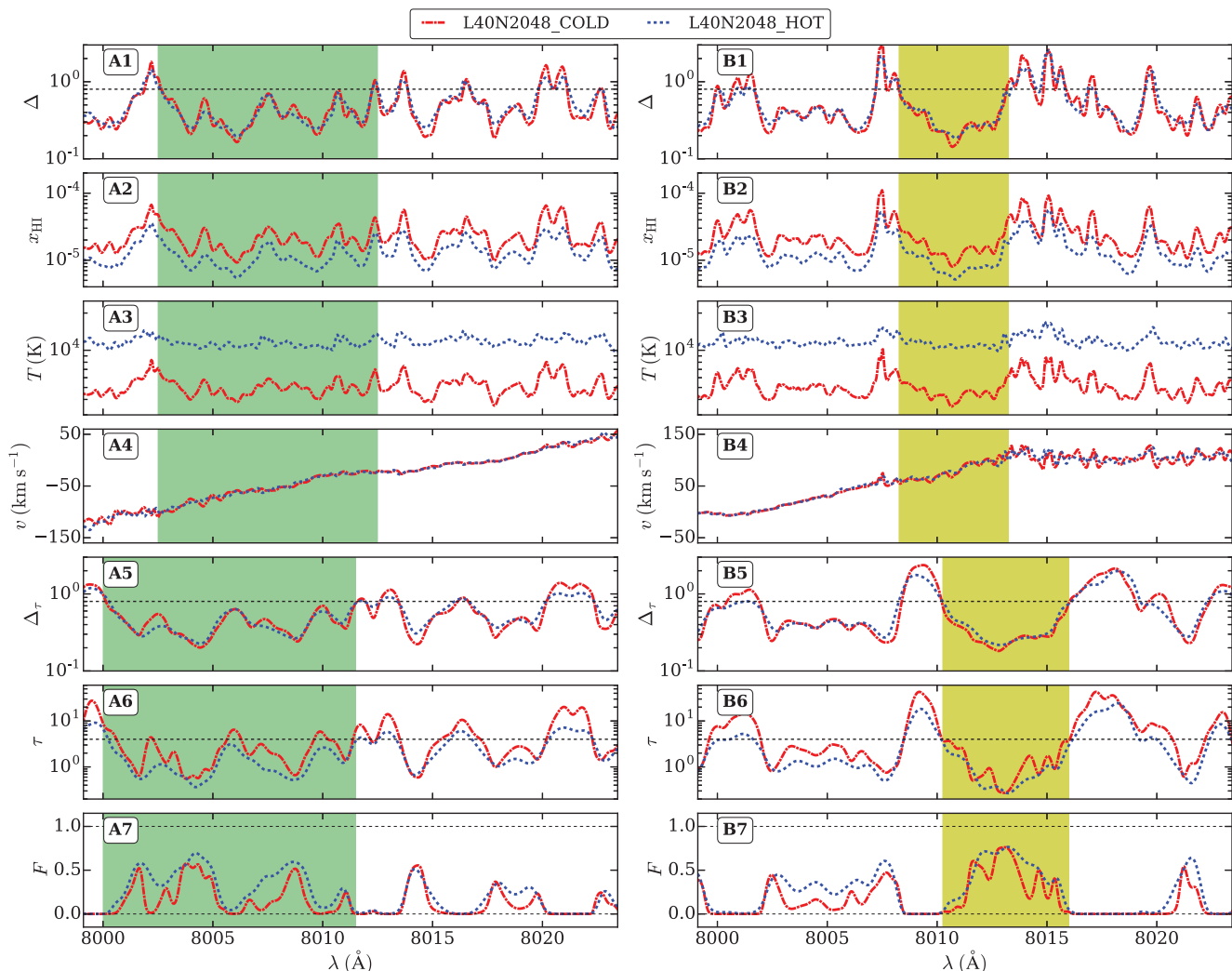


Figure 4. Examples of transmission spikes in optically thin simulations showing the complex structure of the spikes and the dependence on the thermal state of IGM. The figure shows a line-of-sight comparison of overdensity (Δ , panel A1), HI fraction (x_{HI} , A2), temperature (T , A3), peculiar velocity (v , A4), optical depth weighted overdensity (Δ_τ , A5), HI Ly α optical depth (τ , A6), and transmitted Ly α flux (F , A7) for the *cold* (red dot–dashed curve) and the *hot* (blue dotted curve) optically thin simulations. Panels B1–B7 are the same as panel A1–A7 along a different line of sight. The shaded region in panels A7 and B7 show the complex shapes of the spikes in regions where the optical depth is lowest ($\tau_{\text{HI}} \leq 4$, black dashed line in panels A6 and B6). The shapes of the spikes are smoother in the *hot* model due to the larger temperature (panels A3 and B3) and smoother density field (panels A1 and B1) than those in the *cold* model. As a result, the number of components identified by VIPER is smaller in the *hot* model. The transmission spikes also reach larger fluxes in the *hot* model due to the dependence of the HI fraction (panels A2 and B2) on temperature (via the recombination rate). The shift of the shaded region in panels A1–A4 (B1–B4) as compared with panels A5–A7 shows the effect of peculiar velocity on the transmission spikes. The spikes in the simulated spectra occur due to a combination of the effects of underdensity, temperature enhancement, and peculiar velocity as shown in Fig. 2 (Γ_{12} is uniform in the optically thin simulations). The mean transmitted flux has not been rescaled for *hot* and *cold* models in the above examples.

4 CHARACTERIZING THE PROPERTIES OF TRANSMISSION SPIKES IN OPTICALLY THIN SIMULATIONS

4.1 Voigt profile fitting of the inverted flux $1 - F$

The shape of absorption features is usually characterized by Voigt profiles defined by three parameters: (i) the centre of absorption lines (λ_c), (ii) the HI column density (N_{HI}), and (iii) the width of the absorption (b) features. Most of the absorption features in the high- z ($z \sim 6$) Ly α forest are saturated ($F \sim 0$) and strongly blended. It is well known that Voigt profile decompositions are highly degenerated for saturated lines and very sensitive to systematic errors due to continuum fitting and treatment of noise

properties (Webb & Carswell 1991; Fernández-Soto et al. 1996). The inverted transmitted flux, $1 - F$, however, becomes similar in appearance to the absorption features in the Ly α forest at lower redshift, where Voigt profile fitting is much less problematic. For convenience, we have thus fitted Voigt profiles to $1 - F$, building on existing experience with Voigt profile decomposition of complex blended spectral profiles. At the redshift, we consider here that the transmission spikes are observed to be unsaturated, so effectively we use our Voigt profile Parameter Estimation Routine (VIPER, Gaikwad et al. 2017b) to fit multicomponent Voigt profiles to the transmission profiles. Similar to absorption lines, a simple, isolated, and symmetric spike is fitted by three parameters: (i) a spike centre (λ_c), (ii) the logarithm of the pseudo-column density (denoted by

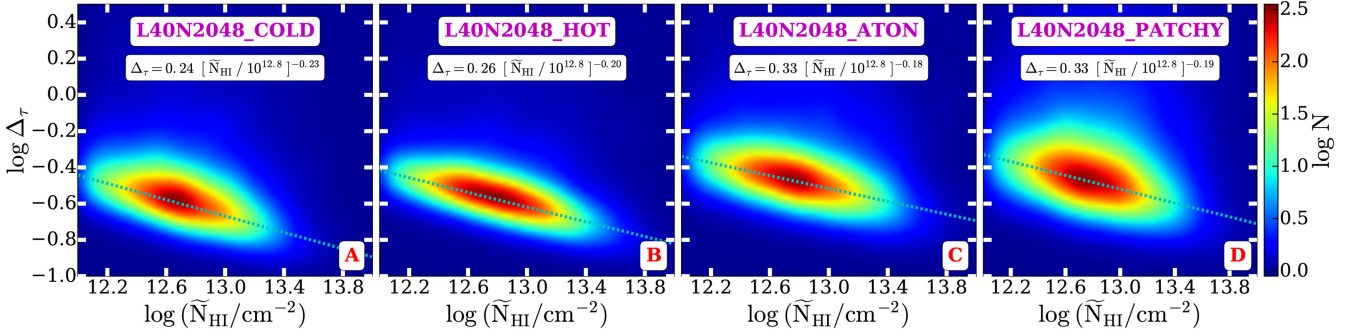


Figure 5. Panels A, B, C, and D show the correlation of optical depth weighted overdensity (Δ_τ) with the pseudo-column density ($\log \tilde{N}_{\text{HI}}$) of transmission spikes in, respectively, the *cold*, *hot*, *aton*, and *patchy* models at $5.5 < z < 5.7$. Irrespective of the model, the spikes correspond to underdensities i.e. $\Delta \sim 0.25$ for $\log \tilde{N}_{\text{HI}} = 12.8$ in the optically thin simulations and $\Delta \sim 0.33$ for $\log \tilde{N}_{\text{HI}} = 12.8$ in the RT simulations. The correlation can be fitted with a straight line (cyan dotted line) and shows good agreement between the various models. The transmission spikes in the RT simulations are produced by regions with slightly larger densities ($\Delta \sim 0.33$) than those in the optically thin simulations ($\Delta \sim 0.25$). This is due to the spatial fluctuations in the photo-ionization rate and temperature that are present in the RT simulations. We discuss the Δ_τ versus $\log \tilde{N}_{\text{HI}}$ correlation for the optically thin and RT simulations in Section 4.2.1 and Section 6.2.1, respectively.

$\log \tilde{N}_{\text{HI}}$), and (iii) a spike width (b). The pseudo-column density is thereby a measure of the deficiency of HI along the sightline where the spike occurs. For example, a larger value of $\log \tilde{N}_{\text{HI}}$ means a large HI deficit and hence a more prominent spike. Our measured $\log \tilde{N}_{\text{HI}}$ are sensitive to the HI photo-ionization rate Γ_{HI} . The interpretation of the other two parameters i.e. λ_c and width of the spikes remains unchanged when we fit $1 - F$. As we show below, the distribution of spike widths is sensitive to the thermal state of the IGM and can be used to constrain the temperature of the IGM.³

Our main aim is to use the distribution of spike widths to constrain the thermal state of the IGM. As we will show later, these are much less sensitive to IGM ionization state and continuum-fitting uncertainties than the heights of the spikes. Note that we rescale the optical depth in different models to match observations as to account for the uncertainty in Γ_{HI} at $5.3 < z < 5.9$ (rescaling is not applied in Fig. 4). We show that such rescaling does not significantly affect the widths of the line in Appendix A.

4.2 The physical properties of the gas probed by transmission spikes

4.2.1 The dependence of spike height on density: Δ_τ versus $\log \tilde{N}_{\text{HI}}$

We now turn to connecting the observed spike shapes to optical depth weighted physical properties of the IGM in the optically thin simulations (see equation 12 in Gaikwad et al. 2017a). In Fig. 5, we show the optical depth weighted overdensity against spike height as measured by (pseudo) column density $\log \tilde{N}_{\text{HI}}$ for the *cold* and *hot* models. In both models, the corresponding overdensity of spikes is $\Delta_\tau < 1$ i.e. most of the spikes occur in underdense regions. Note that applying a rescaling of optical depth to correct for the uncertain amplitude of the UV background results in a systematic increase or decrease of $\log \tilde{N}_{\text{HI}}$. However, the overdensities corresponding to spikes are relatively robust. This is also evident from Fig. 4,

where the spikes in the *hot* and *cold* models correspond to similar overdensities (rescaling is not applied in Fig. 4).

Fig. 5 also illustrates that $\log \tilde{N}_{\text{HI}}$ and Δ_τ are anticorrelated i.e. a larger spike height and higher HI pseudo-column density correspond to smaller overdensity Δ_τ . We quantify the degree of anticorrelation by fitting a straight line of the form $\Delta_\tau = \Delta_0 [\tilde{N}_{\text{HI}} / 10^{12.8}]^\beta$. The normalization ($\Delta_0 = 0.24$ for *cold* and 0.26 for *hot*) and slope ($\beta = -0.23$ for *cold* and -0.20 for *hot*) of the correlation in the two models are in good agreement with each other. This suggests that the thermal state of the gas does not have a strong effect on the $\Delta_\tau - \log \tilde{N}_{\text{HI}}$ correlation when optical depths are rescaled to match observations. Note, however, that the scatter in Δ_τ for a given $\log \tilde{N}_{\text{HI}}$ (e.g. at $\log \tilde{N}_{\text{HI}} \sim 12.6$) correlation is smaller in the *hot* model. This is because the spikes are smoother and hence there is less variation in Δ_τ .

4.2.2 The dependence of spike width on temperature: T_τ versus $\log b$

The widths of the components fitted to the spikes are sensitive to the instantaneous temperature along the sightline (see Figs 1 and 4). Fig. 6 shows the correlation of optical depth weighted temperature (T_τ) with spike width (b) for the *cold* and *hot* models. The range in temperature associated with spikes is small for both models. This is expected as the slope of the TDR (Fig. 3) for both models is relatively flat and the temperature associated with $\Delta < 1$ is relatively constant.

Fig. 6 illustrates that the spike widths are well correlated with temperature. The spike widths are systematically larger in the *hot* model ($\log b \sim 1.3$) than in the *cold* model ($\log b \sim 1.05$). Even though the range in temperature is small ($\delta \log T_\tau \sim 0.1$) for both models, the scatter in $\log b$ is relatively large ($\delta \log b \sim 0.5$). In Section 5.4, we will use the spike width distribution to constrain the temperature of the IGM.

4.2.3 The correlation of spike width and height: $\log b$ versus $\log \tilde{N}_{\text{HI}}$

The relation of absorption line widths with column density and its relation with the thermal state of the gas at $z < 4$ has been widely discussed in the literature (Schaye et al. 1999; Bolton et al. 2014;

³Unlike for absorption lines, there is no direct relation between temperature of the absorbing gas and the width of the spikes, such that $b_{\text{spike}} \neq \sqrt{2k_B T / m}$.

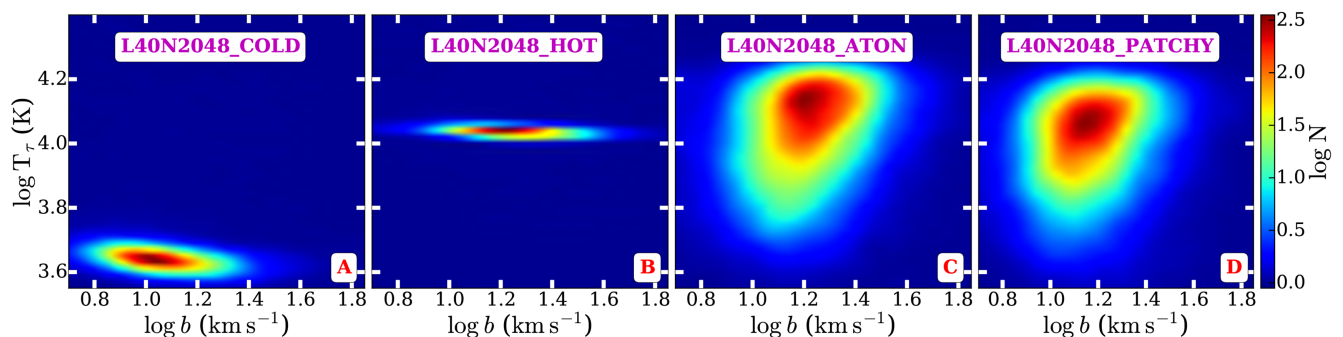


Figure 6. Panels A, B, C, and D show the correlation of optical depth weighted temperature (T_r) with the line-width parameter ($\log b$) of spikes in, respectively, the *cold*, *hot*, *aton*, and *patchy* models at $5.5 < z < 5.7$. The b -parameter and T_r are systematically larger in the *hot* model than the *cold* model. As shown in Fig. 3, T_r is larger in the *aton* model than in the *patchy* model due to the presence of more gas at $\Delta < 1$ and $T < 30\,000$ K in the *aton* model. The scatter in temperature in the RT simulation is much larger than that in optically thin simulations due to the presence of UV background and temperature fluctuations. We discuss the T_r versus ($\log b$) correlation for optically thin and RT simulations in Section 4.2.2 and Section 6.2.2, respectively.

Gaikwad et al. 2017b; Rorai et al. 2017b, 2018; Hiss et al. 2018, 2019). The equivalent relation for the Voigt profile parameters of the transmission spikes in our simulated spectra is compared in Fig. 7 to the observed spectra (white crosses). Fig. 7 shows a strong positive correlation between $\log b$ and $\log \tilde{N}_{\text{HI}}$ for both models. We fit this correlation with a straight line of the form $b = b_0 [\tilde{N}_{\text{HI}} / 10^{12.8}]^\alpha$ with $b_0 = (16.65, 10.93 \text{ km s}^{-1})$ and $\alpha = (0.32, 0.41)$ for the *hot* and *cold* models, respectively. The *hot* model is in significantly better agreement with the observations than the *cold* model. The somewhat flatter slope in the *hot* model is likely due the flatter TDR in the *hot* simulation. Note further that the scatter in $\log \tilde{N}_{\text{HI}}$ is slightly larger in the *hot* model. This is because the spikes are more blended and hence less distinctive (Figs 1 and 4). The scatter in $\log b$ is similar.

In summary, we find strong correlations of the Voigt profile parameters with physical quantities in the optically thin simulations, where : (i) the gas probed by the transmission spikes is typically underdense ($\Delta \sim 0.3$) and (ii) the spike widths (heights) are strongly (anti-) correlated with temperature (density).

5 COMPARING TRANSMISSION SPIKE PROPERTIES IN OBSERVATIONS AND SIMULATIONS

5.1 Characterizing the flux distribution in transmission spikes

Constraints on cosmological and astrophysical parameters from Ly α forest data have been obtained typically by using a variety of statistical measures of the Ly α -transmitted flux and/or Voigt profile decomposition (Storrie-Lombardi, McMahon & Irwin 1996; Penton, Shull & Stocke 2000; McDonald et al. 2000, 2005; Viel, Weller & Haehnelt 2004b; Viel, Bolton & Haehnelt 2009; Becker et al. 2011; Shull, Smith & Danforth 2012). Here, we briefly consider both approaches before focusing on constraints on the thermal state of the IGM from the width distribution of transmission spikes. The transmitted flux-based statistics (such as the probability distribution function and power spectrum) are straightforward to derive from simulations and observations. For the Voigt profile parameter-based statistics, we have fitted Voigt profiles to the inverted transmitted flux, $1 - F$, using VIPER.⁴

⁴Note that as the transmission spikes are generally not ‘saturated’ in $1 - F$, we are effectively fitting Gaussian profiles.

The simulated spectra mimic the observed spectra in terms of S/N and instrumental resolution. VIPER accounts for these effects when determining the best-fitting parameters, the 1σ statistical uncertainty on best-fitting parameters and a significance level for each Voigt component. For deriving the spike statistics, we chose only those Voigt components with relative error on parameters ≤ 0.5 and with a significance level of ≥ 3 . We consider three statistics of the flux distribution in the transmission spikes that are sensitive to astrophysical parameters i.e. Γ_{HI} , T_0 , and γ (for a given cosmology), which are discussed below.

5.2 Statistics of the flux distribution in transmission spikes

5.2.1 Spike width (b-parameter) distribution function

For absorption features, the line width distribution is frequently used as a diagnostic for the gas temperature, turbulence, and the impact of stellar and AGN feedback on the IGM at $z < 5$ (Rauch et al. 1996; Tripp et al. 2008; Oppenheimer & Davé 2009; Muzahid et al. 2012; Gaikwad et al. 2017a; Nasir et al. 2017; Viel et al. 2017). By contrast, the width of the individual spikes is not a direct measure of the temperature of the low-density gas (i.e. $b_{\text{spike}} \neq \sqrt{2k_B T/m}$). Nevertheless, we find that the width of transmission spike components is systematically larger if the temperature of the IGM is larger.⁵

5.2.2 Pseudo Column Density Distribution Function (pCDDF)

Similar to the HI column density distribution function (CDDF) at low redshift, we define the pseudo-CDDF (pCDDF) as the number of spikes with a pseudo column density in the range $\log \tilde{N}_{\text{HI}}$ to $\delta \log \tilde{N}_{\text{HI}}$ in the redshift interval z to $z + \delta z$ (Schaye et al. 2000; Shull et al. 2012). We calculate the pCDDF in 7 $\log \tilde{N}_{\text{HI}}$ bins centred at 12.7, 13.1, ..., 13.9 with $\text{dlog } \tilde{N}_{\text{HI}} = 0.2$. This choice of bins is motivated by the S/N and resolution of the observed spectra. The pCDDF characterizes the height and number of spikes in a given redshift bin and is sensitive to the thermal and ionization parameters of the IGM.

⁵Since spikes trace cosmic voids, the spike width distribution could in principle also be sensitive to cosmological parameters e.g. h , Ω_Λ , σ_8 , and n_s . In this work, we used the spike width distribution to constrain the thermal state of IGM for a given cosmology.

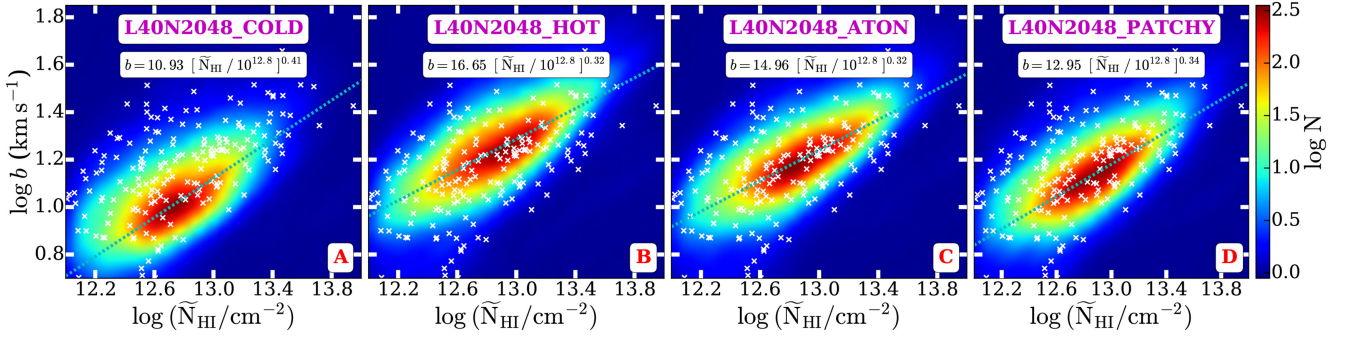


Figure 7. Panels A, B, C, and D show the correlation of the line-width parameter ($\log b$) with the pseudo-column density ($\log \tilde{N}_{\text{HI}}$) of the transmission spikes in, respectively, the *cold*, *hot*, *aton*, and *patchy* models at $5.5 < z < 5.7$. The correlation is fitted with a straight line (cyan dotted line). The $\log b$ -parameter at fixed $\log \tilde{N}_{\text{HI}}$ is systematically larger in the *hot* model ($b \sim 16.65 \text{ km s}^{-1}$ at $\log \tilde{N}_{\text{HI}} = 12.8$) than in the *cold* model ($b \sim 10.93 \text{ km s}^{-1}$ at $\log \tilde{N}_{\text{HI}} = 12.8$). The slope of the correlation is steeper for the *cold* (~ 0.41) model compared to the *hot* model (~ 0.32). The b -parameters in the *aton* model ($b \sim 14.96 \text{ km s}^{-1}$ at $\log \tilde{N}_{\text{HI}} = 12.8$) are systematically larger than in the *patchy* model ($b \sim 12.95 \text{ km s}^{-1}$ at $\log \tilde{N}_{\text{HI}} = 12.8$). This is because temperatures in the *aton* model are larger than in the *patchy* model for $\Delta < 1$ (see Fig. 6). The white crosses show the scatter in $\log b$ and $\log \tilde{N}_{\text{HI}}$ in the observed spectra. We discuss the ($\log b$) versus $\log \tilde{N}_{\text{HI}}$ correlation for optically thin and RT simulations in Section 4.2.3 and Section 6.2.3, respectively.

5.2.3 Transmitted flux power spectrum (FPS)

The transmitted FPS is frequently used to constrain cosmological (McDonald et al. 2000; Meiksin & White 2004; Viel et al. 2004b) and astrophysical parameters (especially, parameters describing the thermal state; Boera et al. 2019; Walther et al. 2019). The FPS is a measure of the clustering of the pixels in transmission spikes. One can also study the two-point correlation of spikes (see e.g. Maitra et al. 2019). However, due to the limited number of observed QSOs and the smaller number of spikes detected per sightline, the two-point correlation function of spikes is rather noisy. It is important to note that, unlike the pCDDF or the spike width distribution, the FPS is a transmitted flux-based statistic that does not require us to fit the spikes. The FPS can, however, be reliably estimated for only a limited range of scales because of finite length of the spectra and other systematic effects. The smallest k (larger scales) modes are limited by the length of the simulation box and continuum-fitting uncertainties of the observed spectra. The largest k modes (smallest scales) on the other hand are limited by the resolution of the instrument and the noise properties (S/N and noise correlation scale if non-Gaussian) of the observed spectra. To account for this, we calculate the FPS in the range $0.01 \leq k (\text{s km}^{-1}) \leq 0.237$ with bin width $\delta \log k = 0.125$ (Kim et al. 2004).⁶

5.2.4 Error estimation

We estimate the error for the spike and flux statistics from the simulation using an approach similar to that in Rollinde et al. (2013) and Gaikwad et al. (2018). For this, we generate samples of five simulated Ly α forest spectra corresponding to five observed QSO spectra with the same observational property i.e. redshift path-length, noise property, number of pixels etc. A collection of five spectra constitutes a single mock sample. We generate 80 such mock samples and compute the covariance matrix for each statistics. We find that the covariance matrix is converged and dominated by diagonal terms for all the statistics.

We have also estimated the covariance matrix from observations using a bootstrap method. Here, we find that the off-diagonal terms of the covariance matrix estimated with the bootstrap method are not

converged. The bootstrap method (diagonal terms) underestimates the error by ~ 15 percent as compared to those estimated from the simulations. Throughout this work, we use bootstrap errors increased by a corresponding factor for each statistics.

5.3 Transmission spike statistics: optically thin simulations versus observations

Fig. 8 compares the spike width distribution, pCDDF and FPS from observations with that of the optically thin simulations for three different redshift bins centred at $z = (5.4, 5.6, 5.8)$.⁷ The corresponding residuals suggest a good level of agreement between the *default* model and observations for all three statistics. The residuals for the *hot* model with $T_0 \sim 11000 \text{ K}$ and $\gamma \sim 1.2$ are somewhat larger. Overall, the three statistics for the *default* and *hot* models are in noticeably better agreement than those for the *cold* model, with differences in the Doppler parameter distribution being most pronounced where agreement with the *default* model is significantly better than with both the *hot* and *cold* models. The *cold* model also predicts more power on small scales, as well as a larger number of spikes with small $\log \tilde{N}_{\text{HI}}$ than observed, and is clearly the model that is least consistent with the observations. We further quantify the degree of agreement between models and observation in Appendix D.

5.4 Constraining thermal parameters with optically thin simulations

In the optically thin simulations, there is a well-defined TDR in underdense and moderately overdense regions. It is thus a common practice to study the effect of the thermal state on flux statistics by imposing different TDRs by rescaling temperatures (Hui & Gnedin 1997; Rorai et al. 2017b, 2018). In Appendix B, we use such rescaling to show how the three flux statistics we consider here depend on thermal parameters T_0 and γ and the photo-ionization rate and demonstrate that it is the width distribution of the transmission spikes which is most sensitive to the thermal state of the gas. We

⁶The smallest k mode corresponds to a scale of $\sim 10h^{-1} \text{ cMpc}$.

⁷The mean transmitted flux in *hot*, *cold*, and *default* models is matched to that in the observed spectra to account for the uncertainty in the continuum placement and UV background amplitude, see Appendix A.

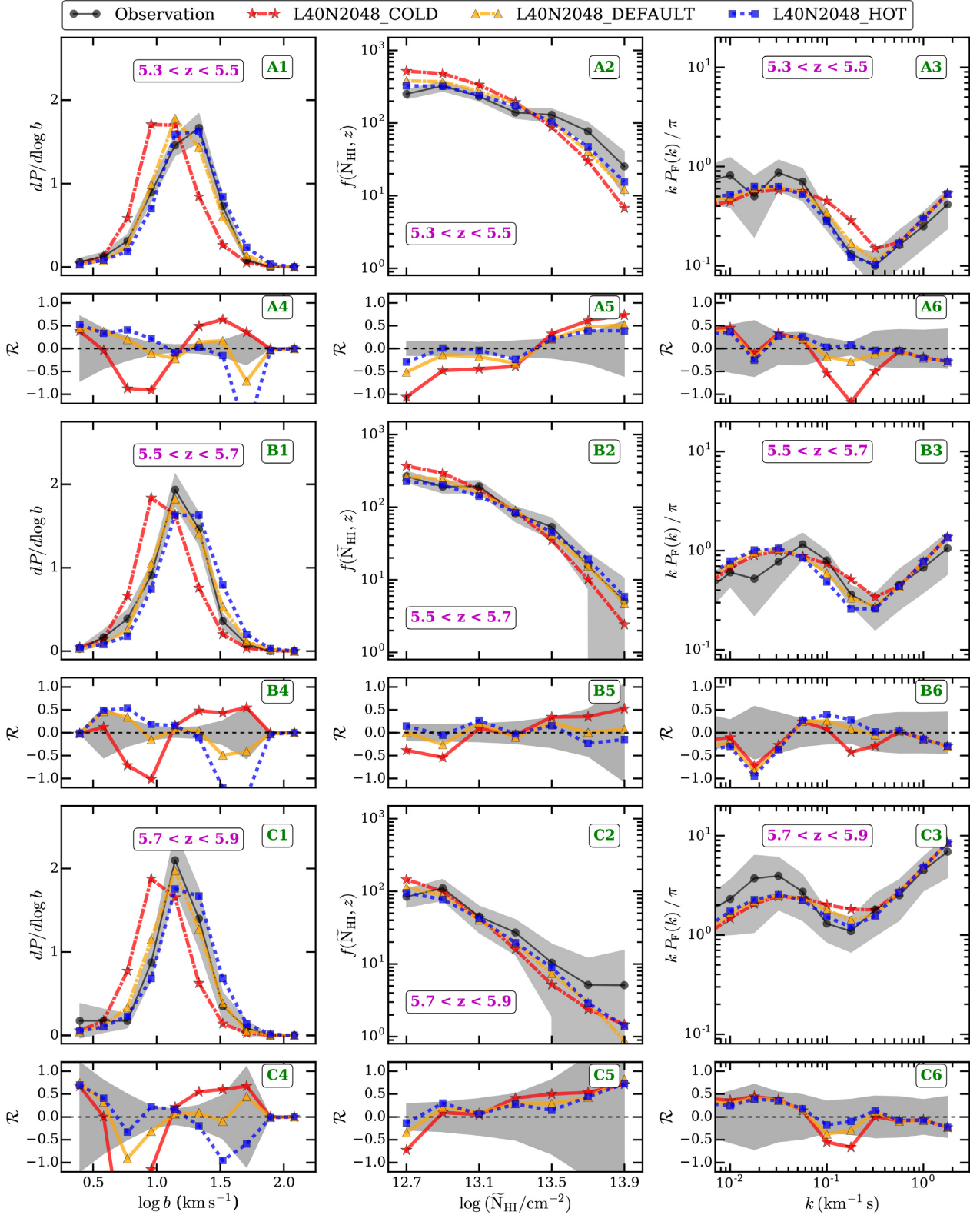


Figure 8. Panels A1, A2, and A3 show a comparison of spike width distribution, pCDDF and FPS from observations (black circles) with those from *cold* (red stars), *default* (orange triangles), and *hot* (blue squares) optically thin simulations at $5.3 < z < 5.5$. The 1σ uncertainties are estimated from the simulated spectra and are shown by the grey-shaded regions. Panels A4, A5, and A6 show the corresponding residuals between the models and observations. The grey-shaded region in panels A4–A6 corresponds to the grey-shaded region in panels A1–A3. Panels B1–B6 and C1–C6 are similar to panels A1–A6 except for the different redshift range, $5.5 < z < 5.7$ and $5.7 < z < 5.9$, respectively. Note that the *hot* and *default* models are in better agreement with observations than the *cold* model at all redshifts. The agreement between model and observed data is discussed quantitatively in Appendix D. The spike statistics in the *default* model are very close to those of the best-fitting model obtained by varying T_0 and γ in Section 5.4.

further show that, for the reionization and thermal history models we consider in this work, the spike statistics are only very weakly affected by pressure (Jeans) smoothing at the typical gas densities probed by the Ly α transmission spikes (Gnedin & Hui 1998; Theuns, Schaye & Haehnelt 2000; Peebles et al. 2010; Kulkarni et al. 2015; Lukić et al. 2015; Nasir, Bolton & Becker 2016; Maitra et al. 2019; Wu et al. 2019).

We use the spike width distribution to obtain an estimate of the best-fitting values and uncertainty for the thermal parameters.⁸ We vary T_0 and γ by assuming a TDR of the form $T = T_0 \Delta^{\gamma-1}$ for $\Delta < 10$ and $T = T_0 10^{\gamma-1}$ for $\Delta \geq 10$. We use the Δ and v fields from the optically thin *default* model, which falls in between the *cold* and *hot* models. We vary T_0 between 6000 K and 20000 K in steps of 500 K and γ between 0.4 and 2.0 in steps of 0.05. For each model, we (i) compute the Ly α -transmitted flux, (ii) post-process the transmitted flux to match observations, (iii) fit the inverted transmitted flux with Voigt profiles, and (iv) compute spike statistics. We use 2000 sightlines for each model. Fig. 9 shows the 1σ constraints on $T_0 - \gamma$ in three redshift bins.⁹ Fig. 9 also shows the marginal distributions of T_0 and γ . Table 3 summarizes the best-fitting values and uncertainty on T_0 and γ values under the assumption that the IGM is optically thin. The uncertainty on the T_0 and γ measurement accounts for the uncertainty due to continuum fitting, mean flux, and Jeans smoothing effects (see Appendices A and B). The best-fitting values and uncertainty on T_0 and γ are consistent with each other within 1σ for the three redshift bins. As the spikes are probing predominantly gas at densities lower than the mean, the inferred values for T_0 and γ are strongly correlated. We will come back to this in Appendix B.

Fig. 10 compares the evolution of T_0 and γ from this work with a variety of measurements in the literature (Becker et al. 2011; Bolton et al. 2012, 2014; Boera et al. 2014; Rorai et al. 2017b; Hiss et al. 2018; Boera et al. 2019; Walther et al. 2019).¹⁰ Theoretical models for the evolution of T_0 and γ from Puchwein et al. (2019) and Haardt & Madau (2012) are shown by the dashed and dotted curves, respectively.¹¹ The T_0 and γ evolution in these models is obtained for a uniform but time-evolving Ultra-Violet Background (UVB) and assuming non-equilibrium ionization evolution. Our T_0 and γ constraints in the redshift range $5.3 < z < 5.9$ are consistent with the corresponding evolution of the *default* model in Puchwein et al. (2019) within 1σ .

Fig. 10 also shows that the T_0 evolution in the *hot* (*cold*) model is systematically larger (smaller) than in the corresponding *default* model. The errors on T_0 and γ account for the statistical and systematic uncertainty (mainly due to continuum fitting). It is interesting to note that the uncertainty on our T_0 measurement is smaller than the T_0 evolution spanned by the *hot* and *cold* models. Our T_0 (γ) measurements are higher (lower) than the measurement of Walther et al. (2019). Note, however, that the T_0 and γ constraints in Walther et al. (2019) are obtained using the FPS whereas we

obtained the T_0 and γ constraints from the spike width distribution that is less sensitive to continuum placement and Γ_{HI} uncertainty (see Appendix A). Further note that the best-fitting T_0 and γ values obtained for the three redshift bins are close to those in the *default* optically thin simulation.

Fig. 8 also shows that the FPS and pCDDF statistics of the *default* model are consistent with the observations within 1.5σ . The best-fitting model obtained by matching the spike width distribution with observations should therefore also have FPS and pCDDF statistics in good agreement with observations. Our γ constraints ($\gamma \sim 1.2$) correspond to a TDR that is moderately steeper than isothermal. However, as we show later, there is no single power-law TDR at the redshift of our analysis since the reionization is a patchy inhomogeneous process with different regions reionizing at different times. At $5.3 < z < 5.9$, γ is therefore not well defined in our RT simulations (Keating et al. 2018). In summary, the T_0 (γ) constraints obtained in this work are larger (smaller) than those obtained by Walther et al. (2019). We do not see a significant evolution of T_0 and γ in the redshift range $5.3 < z < 5.9$.

Transmission spikes in optically thin simulations are mainly produced by fluctuations in the density field and the effect of peculiar velocities. Furthermore, the temperature is strongly and tightly correlated with density in optically thin simulations. However, at the redshifts considered here, this almost is certainly not realistic. One would expect a large scatter in temperature for a given density as the reionization process will be inhomogeneous, with different regions ionized at different times (Abel & Haehnelt 1999; Miralda-Escudé, Haehnelt & Rees 2000; Trac et al. 2008; Choudhury, Haehnelt & Regan 2009). The resulting spatial fluctuations in the amplitude of the UVB and the TDR are not present in optically thin simulations.¹² However, as shown in Section 2.3, transmission spikes can also be produced by fluctuations in the UVB amplitude and/or temperature. Including these RT effects is therefore particularly relevant if reionization ends as late as suggested by the large spatial fluctuations in the Ly α forest opacity (Keating et al. 2019; Kulkarni et al. 2019b).

6 FULL RADIATIVE TRANSFER SIMULATIONS

6.1 The radiative transfer simulations in the Sherwood–Relics simulation suite

In addition to the optically thin simulations discussed in Section 3.1, we have also performed post-processed RT simulations and hybrid RT/hydrodynamical simulations as part of the Sherwood–Relics simulation suite. The former simulations model patchy reionization by performing the RT in post-processing on optically thin simulations. This captures many aspects of patchy reionization such as large spatial fluctuations in the photo-ionization rate and temperature but misses the hydrodynamic response of the IGM to the heating and can thus not accurately predict spatial variations in the pressure smoothing or the distribution of shock-heated gas. The hybrid simulations aim to capture these aspects as well.

The post-processed RT simulations were performed with the GPU-accelerated ATON code in Aubert & Teyssier (2008), which uses a moment-based RT scheme along with the M1 closure relation. The advection of the radiation was performed using the full speed

⁸We find that the FPS and pCDDF statistics are sensitive to continuum fitting uncertainty and Γ_{HI} , whereas the spike width distribution is less sensitive to continuum placement and Γ_{HI} (see Appendix A).

⁹To a good approximation, the likelihood function is Gaussian distributed on $T_0 - \gamma$ grids. See Appendix C for details.

¹⁰Bolton et al. (2012) measure T_0 in QSO proximity regions at $z \sim 6$. Their T_0 constraint including (excluding) a model for the He II photo-heating by the QSOs is shown by green circles (blue squares) in Fig. 10.

¹¹The T_0 and γ evolution in Khaire & Srianand (2015), Khaire & Srianand (2019), and Faucher-Giguere (2019) is similar to that in the Haardt & Madau (2012) UVB model at $z > 5$.

¹²For optically thin simulations, the variation in temperature along a sightline is closely coupled to the variation in the density field.

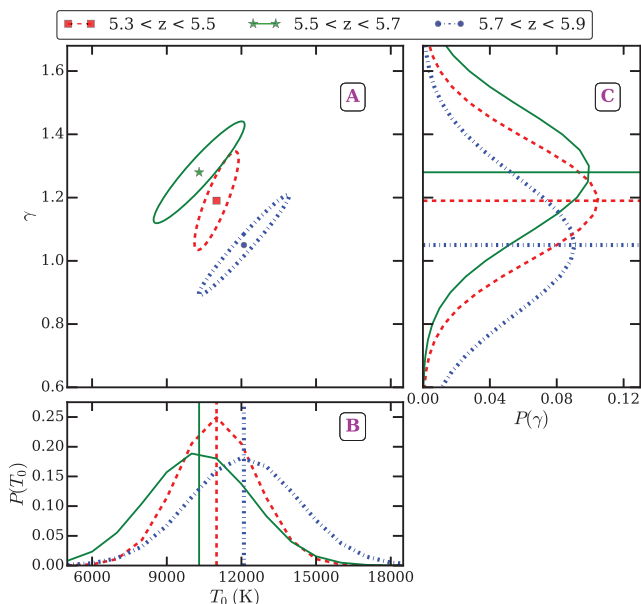


Figure 9. Panel A shows 1σ constraints on T_0 and γ obtained by comparing the transmission spike width distribution from optically thin simulations with observations at $5.3 < z < 5.5$ (red dashed curve), $5.5 < z < 5.7$ (green solid curve), and $5.7 < z < 5.9$ (blue dotted curve). T_0 and γ are varied in post-processing assuming a power-law TDR (the effect of Jeans smoothing is small, see Fig. B5 in the Appendix). Panels B and C show the marginal distributions for T_0 and γ , respectively. The best-fitting T_0 and γ for $5.3 < z < 5.5$ are shown by the red square in panel A and red dashed lines in panels B and C, respectively. Corresponding best-fitting values for $5.5 < z < 5.7$ and $5.7 < z < 5.9$ are shown by the green star and solid line and blue circle and dotted line, respectively.

Table 3. Constraints on $T_0 - \gamma$ from optically thin simulations.

Redshift	$T_0 \pm \delta T_0$	$\gamma \pm \delta \gamma$
$5.3 < z < 5.5$	11000 ± 1600	1.20 ± 0.18
$5.5 < z < 5.7$	10500 ± 2100	1.28 ± 0.19
$5.7 < z < 5.9$	12000 ± 2200	1.04 ± 0.22

of light and a single frequency bin for all ionizing photons. Ionizing sources were inserted into dark matter haloes as in Kulkarni et al. (2019b). The (mean) energy of ionizing photons was assumed to be 18.6 eV. In the following, we will refer to the post-processed RT simulation performed on top of our *default* optically thin simulation by the term *aton* simulation. It used 2048^3 cells in the $(40 h^{-1} \text{ Mpc})^3$ box and hydrogen reionization completes at $z \approx 5.2$, consistent with the late reionization history found to be favoured by large-scale Ly α forest fluctuations (Kulkarni et al. 2019b).

The hybrid RT/hydrodynamical simulation, referred to as the *patchy* simulation, takes the reionization redshift and HI photo-ionization rate maps produced in the *aton* simulation as inputs. These are fed to our modified version of P-GADGET-3, where they are used in the non-equilibrium thermochemistry solver instead of an external homogeneous UV background model. To obtain consistent density and radiation fields, we use the same initial conditions as in the *default* optically thin simulation on which the *aton* run is based. At each time-step, for each SPH particle we check whether it resides in a region in which reionization has already begun. This is assumed to be the case if the ionized fraction in the corresponding cell of

the *aton* simulation has exceeded 3 percent. All particles located in such regions are assumed to be exposed to an ionizing radiation field, which is obtained by interpolating the Γ_{HI} maps produced by *aton* in redshift and reading out the value of the cell containing the particle. This value is then adopted for Γ_{HI} in the non-equilibrium thermochemistry solver. The HI photo-heating rate is computed from Γ_{HI} assuming the same mean ionizing photon energy, 18.6 eV, as in *aton*. As we do not follow He I and He II ionizing radiation separately, we use a few simple assumptions to set their photo-ionization and heating rates. For He I, we use the same photo-ionization rate as for HI, but we adopt a photo-heating rate that is 30 percent larger than that of HI. For He II, we use the rates of the *fiducial* UV background model of Puchwein et al. (2019). This hybrid method results in ionized regions and inhomogeneous photo-heating that closely match those in the parent RT run, while at the same time following the hydrodynamics and hence including consistent pressure smoothing, as well as shock heating.

6.2 The thermal state of the gas in full radiative transfer simulations

The main difference in the RT simulation is that there are large spatial variations in the TDR (Trac et al. 2008; Keating et al. 2018; Kulkarni et al. 2019b). In panels C and D of Fig. 3, we can compare the TDRs from the *aton* and *patchy* RT simulations to the optically thin simulations in panels A and B. Unlike the optically thin simulations, the TDR in the RT simulations at $\Delta < 10$ cannot be described by a single power law (Bolton, Meiksin & White 2004). The regions that have been ionized most recently have a flat TDR while regions that have been ionized earlier have progressively steeper TDRs. In the redshift range considered here, there are also still significant spatial fluctuations in the amplitude of the UVB. As a result, the variation in temperature for a given $\Delta < 10$ is large. A crucial difference between the *aton* and *patchy* simulations is also evident in Fig. 3. The *aton* simulation does not account self-consistently for shock heating of the gas. There is thus much less gas with $T > 30\,000$ K in the *aton* simulation than in the *patchy* simulation. As a consequence, there is less gas with $\Delta < 10$ in the temperature range described by two straight lines (see Fig. 3) in the *patchy* simulation. As we will show later, this has the effect of producing slightly larger spike widths in the *aton* simulations.

Table 2 also shows the physical effects responsible for the occurrence of spikes in the *aton* and *patchy* RT simulations. Similar to the optically thin simulations, most of the spikes (~ 89 per cent) in the *aton* and *patchy* simulations occur in underdense regions and for ~ 18 per cent of spikes, the gas shows a diverging velocity field along the sightline. However, in contrast to optically thin simulations, around 50 per cent of spikes show an enhancement of Γ_{HI} and temperature. Note here that the recent observations of high redshift Lyman alpha emitters and Lyman break galaxies suggest that the transmission spikes are spatially correlated with the ionizing radiation escaping these galaxies (Meyer et al. 2019). Thus, for the transmission spikes in the full RT simulations, all the physical processes discussed in Section 2.3 and Fig. 2 contribute to the occurrence of spikes.

6.2.1 Dependence of spike height on density: Δ_τ versus $\log \tilde{N}_{\text{HI}}$

In Fig. 5, we compare the dependence of Δ_τ on $\log \tilde{N}_{\text{HI}}$ for the *aton* and *patchy* simulations to the optically thin *cold* and *hot* simulations. Similar to the optically thin simulations (Fig. 5), Δ_τ

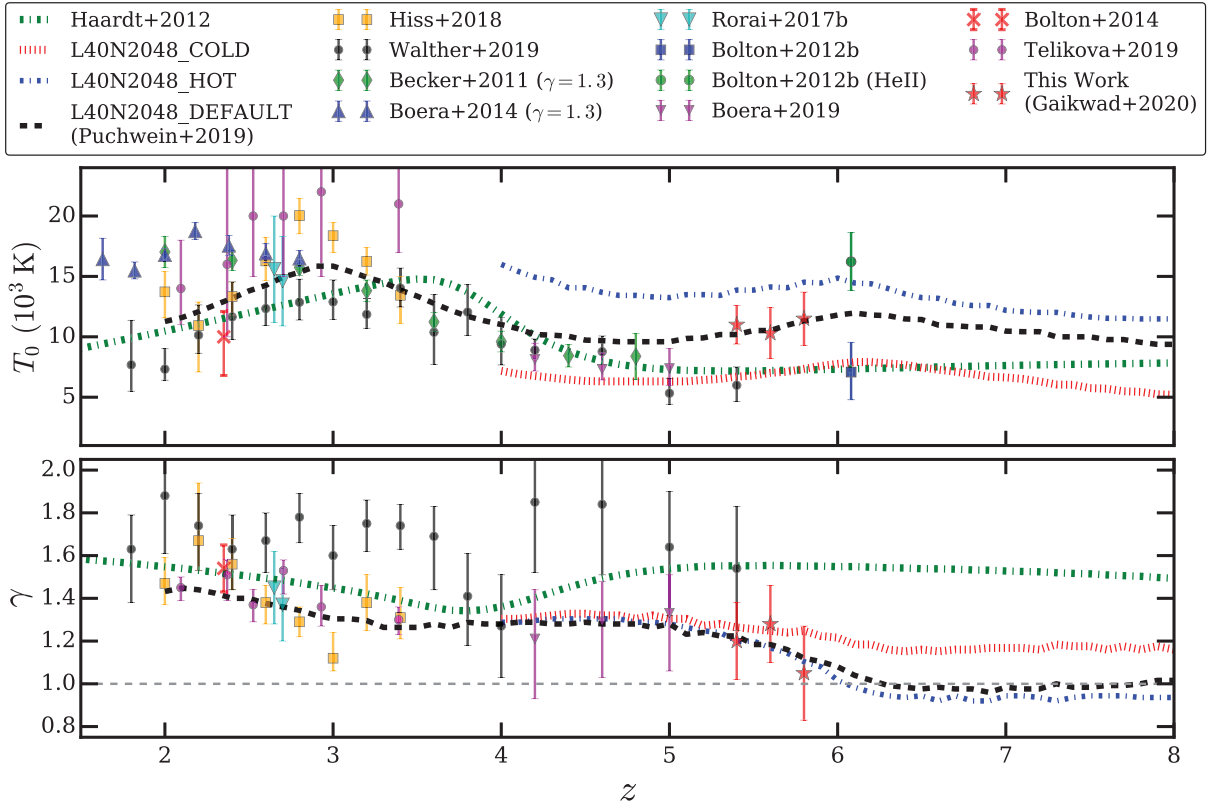


Figure 10. The evolution of thermal parameters T_0 and γ from the literature and in this work (red stars with error bars) is shown in the top and bottom panels, respectively (Becker et al. 2011; Bolton et al. 2012, 2014; Boera et al. 2014; Rorai et al. 2017b; Hiss et al. 2018; Boera et al. 2019; Telikova et al. 2019; Walther et al. 2019). Note that the temperature constraints from Becker et al. (2011) and Boera et al. (2014) are not measured at the mean density and have therefore been scaled to a T_0 value assuming a TDR with slope $\gamma = 1.3$. The T_0 and γ evolution in the *hot*, *default*, and *cold* Sherwood–Relics simulations is shown by the blue dash–dotted, black dashed, and red dotted curves, respectively. The corresponding T_0 and γ evolution in the Haardt & Madau (2012) UVB synthesis model is shown by a green dotted curve. This T_0 and γ evolution is obtained by assuming a uniform UVB and solving for the non-equilibrium ionization evolution (Haardt & Madau 2012; Puchwein et al. 2019). Our constraints on T_0 and γ are consistent within 1σ with Puchwein et al. (2019).

and $\log \tilde{N}_{\text{HI}}$ are anticorrelated. The normalization (Δ_0) and slope (β) are similar in both simulations. The Δ_0 (β) in the RT simulations are slightly larger (smaller) than the optically thin simulations. The spikes (irrespective of $\log \tilde{N}_{\text{HI}}$) in the RT simulations are produced from underdensities somewhat larger than in the optically thin simulations. This is expected, as spikes (at a given $\log \tilde{N}_{\text{HI}}$) in the RT simulations are produced by all four physical effects we discussed previously, i.e. fluctuations in density, peculiar velocity, UVB, and temperature. Fig. 5 also shows that the scatter in Δ_τ (at a given $\log \tilde{N}_{\text{HI}}$) is larger in the RT simulations due to fluctuations in UVB, temperature, and pressure-smoothing effects. Note, however, that in all simulations, the spikes occur in underdense regions with $\Delta < 1$.

6.2.2 Dependence of temperature on spike width: T_τ versus b

Fig. 6 compares the dependence of optical depth weighted temperature (T_τ) on spike widths (b -parameter) for the RT simulations with that in the optically thin simulations. Unlike the optically thin simulations, the RT simulations show a large scatter in temperature for a given spike width due to fluctuations in the UVB amplitude and temperature. Furthermore, the temperature in the *patchy* simulation is smaller than in the corresponding *aton* simulation. This is because (i) the amount of gas with $\Delta < 1$ and $T < 30\,000$ K is larger in the *patchy* simulation and (ii) due to the post-processed nature of the

aton simulation, the (adiabatic) change in the temperature due to changes in density (the $d\Delta/dt$ term) is not accounted. As a result, the spike widths are also slightly smaller in the *patchy* simulations.

6.2.3 The relation of spike width and height: b versus $\log \tilde{N}_{\text{HI}}$

Fig. 7 compares the $b - \log \tilde{N}_{\text{HI}}$ correlation for the *aton* and *patchy* simulations to that in the optically thin simulations. Similar to the optically thin simulations, $\log b$ and $\log \tilde{N}_{\text{HI}}$ are strongly anticorrelated in the RT simulations. The normalization of the correlation b_0 is smaller in the *patchy* (~ 12.95 km s $^{-1}$) simulation than in the *aton* (~ 14.96 km s $^{-1}$) simulation due to the smaller temperature of the gas probed by the transmission spikes in the latter. The slope of the correlation ($\alpha = 0.32$ for *aton* and $\alpha = 0.34$ for *patchy*) and the scatter in the TDR (at $\Delta < 1$ in Fig. 3) is relatively similar for both simulations. It is interesting to note here that α in the RT simulations is similar to that in the *hot* optically thin simulation, while b_0 in the RT simulations is smaller than in the *hot* optically thin simulations. The smaller value of b_0 in the RT simulation is a consequence of fluctuations in UVB amplitude and temperature.

In summary, the RT simulations include the effects of fluctuations in the UVB amplitude and temperature, which are missing in the optically thin simulations. Due to these effects: (i) the TDR in RT simulations cannot be described by a single power law, (ii)

the typical densities responsible for transmission spikes in the RT simulations ($\Delta_0 \sim 0.33$) are slightly larger than in optically thin simulations ($\Delta_0 \sim 0.25$), and (iii) the scatter in temperature and spike width are larger.

6.3 Transmission spike properties: Full radiative transfer simulations versus observations

We now compare the three statistics from the RT simulations with observations in Fig. 11. Each panel is similar to Fig. 8, except that we now use the *aton* and *patchy* simulations. Similar to the optically thin simulations, the mean transmitted flux in the *aton* and *patchy* models is matched to that in the observed spectra to account for the uncertainty in the continuum placement and UV background amplitude. Note that this rescaling has surprisingly little effect on the width of the transmission spikes (see Appendix A). Comparison of Fig. 11 with Fig. 8 shows that the RT simulations are in perhaps even better agreement with the observations than the optically thin simulations at all redshifts. Note, however, that there is still considerable freedom to adjust the overall temperature in both the RT and optically thin simulations. Unfortunately, we therefore do not think that this (marginally) better agreement should be interpreted as (hard) evidence for the spatial variations of the TDR predicted by our RT simulations. The three statistics are furthermore very similar in the *aton* and *patchy* simulations at all redshifts. The spike widths in the *aton* simulations are somewhat larger than in the *patchy* simulations and are in marginally better agreement with observations than in the *patchy* simulations (see Appendix D for a comparison of the goodness-of-fit for the different models). As explained in the previous section, this is due to the effect of slightly higher gas temperatures in the *aton* simulations. Note, however, also that both RT simulations are mono-frequency and the normalization of the temperature distribution predicted by the RT simulations is still somewhat uncertain.

Fig. 12 shows the comparison of the T_0 and γ evolution with that from $T_0 - \gamma$ measured assuming a uniform UVB. Since there is no single power-law TDR in the RT simulations (see Fig. 3), we show a range in T_0 and γ evolution. To obtain this range in T_0 and γ , we find the 16th and 84th percentile temperature in four Δ bins. We then fit a power-law TDR to the 16th and 84th percentile temperature values (see Fig. 3¹³). Fig. 12 shows that the $T_0 - \gamma$ constraints obtained here are consistent with the range in the $T_0 - \gamma$ evolution seen in the *patchy* and *aton* RT simulations.

Thus, quite remarkably the *patchy* simulation based on the self-consistent reionization model of Kulkarni et al. (2019b) that (i) simulates cosmological density and velocity fields, (ii) includes spatial fluctuations in the UV background and TDR, (iii) accounts for the pressure smoothing of gas, and (iv) matches the Thomson scattering optical depth (Planck Collaboration et al. 2018), and also produces transmission spike properties consistent with those in observed high-resolution, high- z QSO absorption spectra. Note, however, that there is still some uncertainty in the post-reionization temperatures in RT simulations (see D’Aloisio et al. 2019; Puchwein et al. 2020, in preparation). With 18.6 eV, the energy of ionizing photons (and thus the post-reionization temperatures) of the simulations used here falls between those in Keating et al. (2019) (17.6 eV) and Kulkarni et al. (2019b) (20.1 eV).

7 CONCLUSIONS

We have explored here for the first time the use of the transmission spikes observed in high- z QSO absorption spectra as a tool to probe the physical state of the IGM near the tail end of hydrogen reionization. We constrain the thermal state of the IGM at $5.3 < z < 5.9$ by comparing the properties of Ly α transmission spikes from a sample of five high-resolution ($v_{\text{FWHM}} \sim 6 \text{ km s}^{-1}$) and high S/N (~ 10) QSO absorption spectra with that from state-of-the-art, high-resolution optically thin simulations run with GADGET-3 (Springel 2005) from the Sherwood and Sherwood–Relics simulation suites, as well as a simulation post-processed with the RT code *aton* (Aubert & Teyssier 2008). The main results of this work are as follows.

(i) In full RT simulations regions with low-density, enhancement in the photo-ionization rate Γ_{HI} , enhancement in temperature, and a diverging peculiar velocity field along the line of sight can all contribute to the occurrence of transmission spikes at high redshift. Most of the spikes (~ 90 percent) in optically thin and RT simulations occur in regions with density $\Delta < 1$. Optically thin simulations do not account for the effect of enhanced temperatures in recently ionized regions and the resulting spatial fluctuations in the temperature–density relation. Due to the assumed spatially homogeneous UV background amplitude, they also do not account for the occurrence of transmission spikes due to enhancements in the photo-ionization rate. About 50 percent of the transmission spikes in our RT simulations show the effect of an enhanced Γ_{HI} and enhanced temperature. In the RT simulation, the transmission spikes are often either due to hot, recently ionized, very underdense regions with a diverging line-of-sight peculiar velocity field or due to somewhat less underdense and colder regions with an enhanced photo-ionization rate.

(ii) The width of the components fitted to the asymmetric and blended transmission spikes is very sensitive to the instantaneous temperature of the gas and is significantly broader in the optically thin *hot* simulation than in the corresponding *cold* simulation. To quantify this, we have fitted multicomponent Voigt profiles to the inverted transmitted flux $1 - F$ in both simulated and observed spectra with our automated code VIPER (Gaikwad et al. 2017b). We derive the transmitted FPS, pCDDF, and spike width (b -parameter) distribution functions for simulated and observed spectra. We show that the spike width distribution is the statistic that is sensitive to the thermal state of the IGM. The dependence of the shape of the FPS and the pCDDF on the temperature of the absorbing gas is somewhat weaker while their normalization is more sensitive to the ionization state/neutral fraction of the IGM.

(iii) We associate the observable properties of spikes with the physical properties of gas in simulations by studying the $\Delta_\tau - \log \tilde{N}_{\text{HI}}$, $T_\tau - b$, and $b - \log \tilde{N}_{\text{HI}}$ correlations. These correlations show that the underdensity of gas associated with spikes is similar i.e. $\Delta_\tau \sim 0.3$ at $\log \tilde{N}_{\text{HI}} \sim 12.8$ in both optically thin and RT simulations. The spike widths in both simulations are sensitive to the temperature of the gas ($b \sim 10.9 \text{ km s}^{-1}$ for $T_0 \sim 7500 \text{ K}$ and $b \sim 16.6 \text{ km s}^{-1}$ for $T_0 \sim 14000 \text{ K}$). However, the temperature scatter for a given density is larger in the RT simulation than in the optically thin simulation. As a result, a significant fraction of spikes in the RT simulations is due to hotter temperatures in recently ionized regions of the Universe.

(iv) We have compared the three observed flux statistics with those derived from our optically thin *hot* and *cold* simulations in three redshift bins. The statistics for the *hot* and *default* models are in significantly better agreement with those from observations in all the three redshift bins. The Doppler parameter distribution,

¹³The T_0 and γ for *aton* and *patchy* models in Fig. 3 are calculated using 5th and 95th percentile.

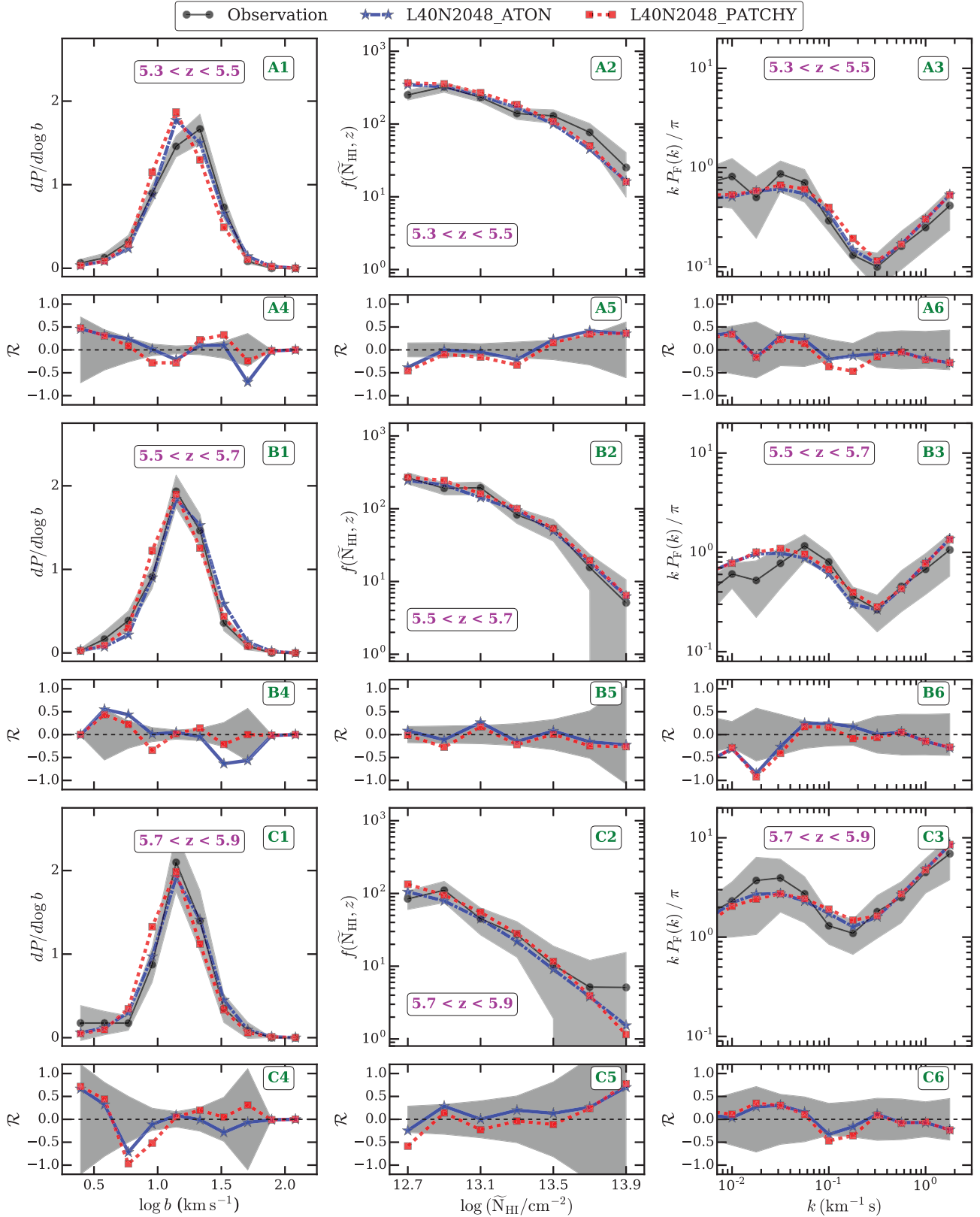


Figure 11. Similar to Fig. 8, except the comparison of spike width distribution, pCDDF and FPS is shown for the *aton* (blue stars) and *patchy* (red stars) RT simulations. The statistics from the RT simulations are in better agreement with observations compared to those from the optically thin simulations (Fig. 8) at all redshifts (see Section 6.3).

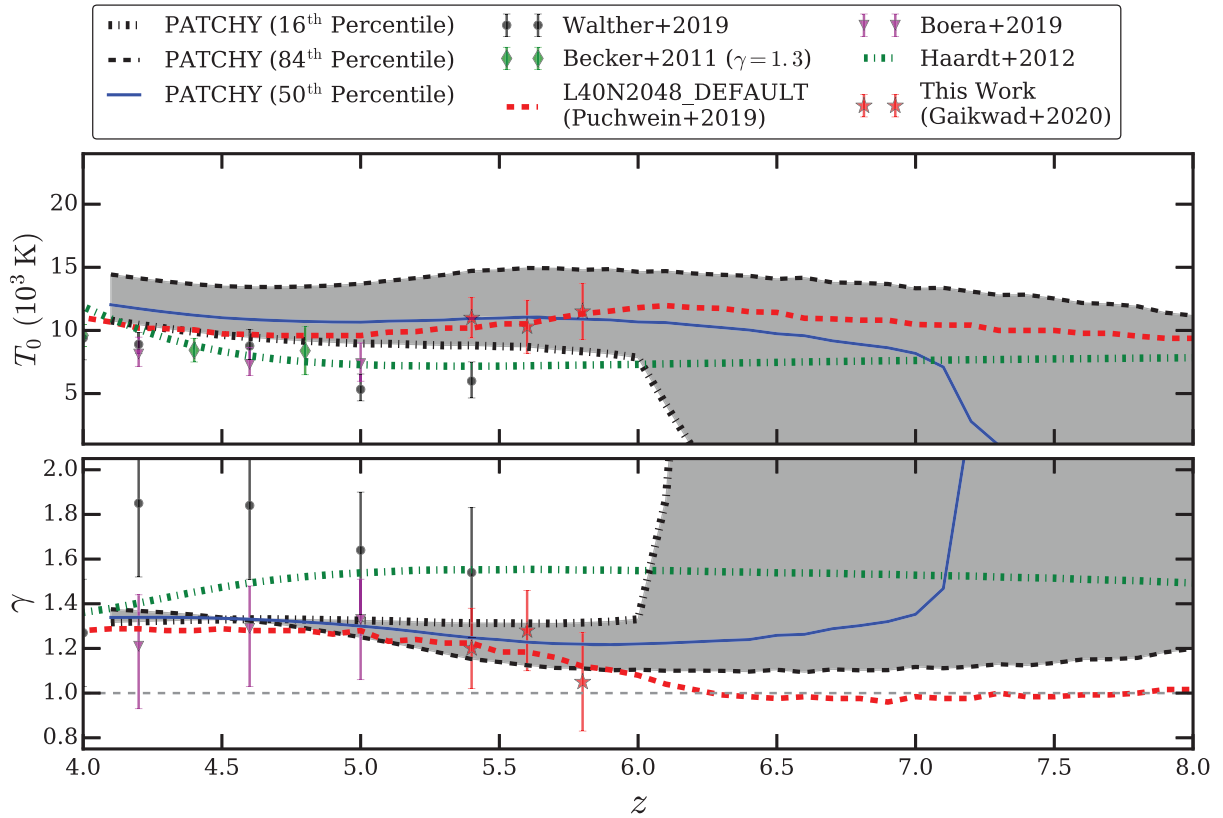


Figure 12. Same as Fig. 10, except the T_0 and γ evolution is shown from the *patchy* RT simulation (shaded region) at $4 \leq z \leq 8$. Since there is no single power-law TDR in the RT simulations (see Fig. 3), the shaded region displays the 16th and 84th percentiles of T_0 and γ (see Section 6.3). For comparison, we also show the T_0 and γ evolution from RT models (50th percentile, blue solid line), the uniform UVB *default* (red dashed line), and Haardt & Madau (2012) (green dotted line) model. The T_0 and γ measured by comparing the observed spike width distribution with that from optically thin simulations are in good agreement with the median T_0 and γ evolution from RT simulations.

which is most sensitive to the instantaneous temperature of the gas, is in significantly better agreement for the *default* model than for both the *cold* and *hot* models. We constrain thermal parameters by varying T_0 and γ in post-processed optically thin simulations. The best-fitting values at $5.3 \leq z \leq 5.5$, $5.5 \leq z \leq 5.7$, and $5.7 < z < 5.9$ are $T_0 \sim 11000 \pm 1600$, 10500 ± 2100 , 12000 ± 2200 K and $\gamma \sim 1.20 \pm 0.18$, 1.28 ± 0.19 , 1.05 ± 0.22 , respectively. We do not find significant evolution in T_0 and γ over $5.3 < z < 5.9$.

(v) We have also compared the three statistics in physically motivated RT simulations with those from observations. Unlike optically thin simulations, RT simulations incorporate spatial fluctuations in the amplitude of the UVB and the TDR. As a result, the scatter in the TDR is large and a single power law cannot describe the TDR in RT simulations. The observed spike statistics in our RT simulation of late reionization with neutral islands persisting to $z \sim 5.3$ are in good agreement (see Appendix D for details) with observations in all three redshift bins.

Our work shows the potential of transmission spike shapes (heights and widths) for constraining the thermal history of the IGM near the tail end of H I reionization, complimentary to other transmitted flux-based methods. In future, a much larger sample of high-resolution, high S/N, and high- z QSO absorption spectra should become available thanks to 30–40 m class optical telescopes. These larger data sets, complemented by further improved RT simulations, promise to put tight constraints on the nature and the exact timing of H I reionization.

ACKNOWLEDGEMENTS

We thank the staff of the Las Campanas and Keck observatories for their help with the observations. M. R. thanks Ian Thompson and Steve Smetman for suggestions for installing a new bandpass filter in the MIKE slit-viewing camera. Support by ERC advanced grant 320596 ‘The Emergence of Structure During the Epoch of reionization’ is gratefully acknowledged. J. S. B. acknowledges the support of a Royal Society University Research Fellowship. G. D. B. was supported by the National Science Foundation through grants AST-1615814 and AST-175140. The Sherwood and Sherwood–Relics simulations were performed with supercomputer time awarded by the Partnership for Advanced Computing in Europe (PRACE) 8th and 16th calls. We acknowledge PRACE for awarding us access to the Curie and Irene supercomputers, based in France at the Trés Grand Centre de Calcul (TGCC). This work also used the Cambridge Service for Data Driven Discovery (CSD3), part of which is operated by the University of Cambridge Research Computing on behalf of the STFC DiRAC HPC Facility (www.dirac.ac.uk). The DiRAC component of CSD3 was funded by BEIS capital funding via STFC capital grants ST/P002307/1 and ST/R002452/1 and STFC operations grant ST/R00689X/1. We also acknowledge the DiRAC Data Intensive service at Leicester, operated by the University of Leicester IT Services. The equipment was funded by BEIS capital funding via STFC capital grants ST/K000373/1 and ST/R002363/1 and STFC DiRAC Operations grant ST/R001014/1. We also thank DiRAC@Durham facility

managed by the Institute for Computational Cosmology on behalf of the STFC DiRAC HPC Facility (www.dirac.ac.uk). The equipment was funded by BEIS capital funding via STFC capital grants ST/P002293/1, ST/R002371/1, and ST/S002502/1, Durham University and STFC operations grant ST/R000832/1. DiRAC is part of the National e-Infrastructure.

REFERENCES

- Abel T., Haehnelt M. G., 1999, *ApJ*, 520, L13
- Aubert D., Teyssier R., 2008, *MNRAS*, 387, 295
- Bañados E. et al., 2016, *ApJS*, 227, 11
- Barnett R., Warren S. J., Becker G. D., Mortlock D. J., Hewett P. C., McMahon R. G., Simpson C., Venemans B. P., 2017, *A&A*, 601, A16
- Becker G. D., Bolton J. S., 2013, *MNRAS*, 436, 1023
- Becker G. D., Bolton J. S., Haehnelt M. G., Sargent W. L. W., 2011, *MNRAS*, 410, 1096
- Becker G. D., Sargent W. L. W., Rauch M., Carswell R. F., 2012, *ApJ*, 744, 91
- Becker G. D., Bolton J. S., Madau P., Pettini M., Ryan-Weber E. V., Venemans B. P., 2015, *MNRAS*, 447, 3402
- Bernstein R., Shtetman S. A., Gunnels S. M., Mochnacki S., Athey A. E., 2003, in Iye M., Moorwood A. F. M., eds, *Proc. SPIE Conf. Ser. Vol. 4841, Instrument Design and Performance for Optical/Infrared Ground-based Telescopes*. SPIE, Bellingham, p. 1694
- Boera E., Murphy M. T., Becker G. D., Bolton J. S., 2014, *MNRAS*, 441, 1916
- Boera E., Becker G. D., Bolton J. S., Nasir F., 2019, *ApJ*, 872, 101
- Bolton J. S., Becker G. D., 2009, *MNRAS*, 398, L26
- Bolton J. S., Haehnelt M. G., 2007, *MNRAS*, 382, 325
- Bolton J., Meiksin A., White M., 2004, *MNRAS*, 348, L43
- Bolton J. S., Haehnelt M. G., Warren S. J., Hewett P. C., Mortlock D. J., Venemans B. P., McMahon R. G., Simpson C., 2011, *MNRAS*, 416, L70
- Bolton J. S., Becker G. D., Raskutti S., Wyithe J. S. B., Haehnelt M. G., Sargent W. L. W., 2012, *MNRAS*, 419, 2880
- Bolton J. S., Becker G. D., Haehnelt M. G., Viel M., 2014, *MNRAS*, 438, 2499
- Bolton J. S., Puchwein E., Sijacki D., Haehnelt M. G., Kim T.-S., Meiksin A., Regan J. A., Viel M., 2017, *MNRAS*, 464, 897
- Bosman S. E. I., Fan X., Jiang L., Reed S., Matsuo Y., Becker G., Haehnelt M., 2018, *MNRAS*, 479, 1055
- Calverley A. P., Becker G. D., Haehnelt M. G., Bolton J. S., 2011, *MNRAS*, 412, 2543
- Carnall A. C. et al., 2015, *MNRAS*, 451, L16
- Chardin J., Puchwein E., Haehnelt M. G., 2017, *MNRAS*, 465, 3429
- Chardin J., Haehnelt M. G., Bosman S. E. I., Puchwein E., 2018, *MNRAS*, 473, 765
- Chehade B. et al., 2018, *MNRAS*, 478, 1649
- Choudhury T. R., Haehnelt M. G., Regan J., 2009, *MNRAS*, 394, 960
- D'Aloisio A., McQuinn M., Maupin O., Davies F. B., Trac H., Fuller S., Upton Sanderbeck P. R., 2019, *ApJ*, 874, 154
- Davies F. B., Hennawi J. F., Eilers A.-C., Lukić Z., 2018, *ApJ*, 855, 106
- Eilers A.-C., Davies F. B., Hennawi J. F., 2018, *ApJ*, 864, 53
- Fan X. et al., 2001, *AJ*, 122, 2833
- Fan X. et al., 2006, *AJ*, 132, 117
- Fan X. et al., 2019, *ApJ*, 870, L11
- Faucher-Giguère A. C., 2019, *MNRAS*, 493, 1614
- Faucher-Giguère C.-A., Lidz A., Hernquist L., Zaldarriaga M., 2008, *ApJ*, 682, L9
- Fernández-Soto A., Lanzetta K. M., Barcons X., Carswell R. F., Webb J. K., Yahil A., 1996, *ApJ*, 460, L85
- Furlanetto S. R., Oh S. P., 2009, *ApJ*, 701, 94
- Gaikwad P., Khaire V., Choudhury T. R., Srianand R., 2017a, *MNRAS*, 466, 838
- Gaikwad P., Srianand R., Choudhury T. R., Khaire V., 2017b, *MNRAS*, 467, 3172
- Gaikwad P., Choudhury T. R., Srianand R., Khaire V., 2018, *MNRAS*, 474, 2233
- Gaikwad P., Srianand R., Khaire V., Choudhury T. R., 2019, *MNRAS*, 490, 1588
- Garaldi E., Gnedin N. Y., Madau P., 2019, *ApJ*, 876, 31
- Garzilli A., Bolton J. S., Kim T.-S., Leach S., Viel M., 2012, *MNRAS*, 424, 1723
- Gnedin N. Y., Hui L., 1998, *MNRAS*, 296, 44
- Gnedin N. Y., Becker G. D., Fan X., 2017, *ApJ*, 841, 26
- Haardt F., Madau P., 2012, *ApJ*, 746, 125
- Haehnelt M. G., Steinmetz M., 1998, *MNRAS*, 298, L21
- Hiss H., Walther M., Hennawi J. F., Oñorbe J., O'Meara J. M., Rorai A., Lukić Z., 2018, *ApJ*, 865, 42
- Hiss H., Walther M., Oñorbe J., Hennawi J. F., 2019, *ApJ*, 876, 71
- Hui L., Gnedin N. Y., 1997, *MNRAS*, 292, 27
- Kakiichi K. et al., 2018, *MNRAS*, 479, 43
- Keating L. C., Puchwein E., Haehnelt M. G., 2018, *MNRAS*, 477, 5501
- Keating L. C., Weinberger L. H., Kulkarni G., Haehnelt M. G., Chardin J., Aubert D., 2020, *MNRAS*, 491, 1736
- Kelson D. D., 2003, *PASP*, 115, 688
- Khaire V. et al., 2019, *MNRAS*, 486, 769
- Khaire V., Srianand R., 2015, *ApJ*, 805, 33
- Khaire V., Srianand R., 2019, *MNRAS*, 484, 4174
- Kim T.-S., Viel M., Haehnelt M. G., Carswell R. F., Cristiani S., 2004, *MNRAS*, 347, 355
- Kulkarni G., Hennawi J. F., Oñorbe J., Rorai A., Springel V., 2015, *ApJ*, 812, 30
- Kulkarni G., Worseck G., Hennawi J. F., 2019a, *MNRAS*
- Kulkarni G., Keating L. C., Haehnelt M. G., Bosman S. E. I., Puchwein E., Chardin J., Aubert D., 2019b, *MNRAS*, 485, L24
- Lidz A., Faucher-Giguère C.-A., Dall'Aglio A., McQuinn M., Fechner C., Zaldarriaga M., Hernquist L., Dutta S., 2010, *ApJ*, 718, 199
- Lukić Z., Stark C. W., Nugent P., White M., Meiksin A. A., Almgren A., 2015, *MNRAS*, 446, 3697
- Maitra S., Srianand R., Petitjean P., Rahmani H., Gaikwad P., Choudhury T. R., Pichon C., 2019, *MNRAS*, 490, 3633
- McDonald P. et al., 2005, *ApJ*, 635, 761
- McDonald P., Miralda-Escudé J., Rauch M., Sargent W. L. W., Barlow T. A., Cen R., Ostriker J. P., 2000, *ApJ*, 543, 1
- McQuinn M., Upton Sanderbeck P. R., 2016, *MNRAS*, 456, 47
- McQuinn M., Lidz A., Zaldarriaga M., Hernquist L., Hopkins P. F., Dutta S., Faucher-Giguère C.-A., 2009, *ApJ*, 694, 842
- McQuinn M., Hernquist L., Lidz A., Zaldarriaga M., 2011, *MNRAS*, 415, 977
- Meiksin A., White M., 2004, *MNRAS*, 350, 1107
- Meyer R. A. et al., 2020, *MNRAS*, 494, 1560
- Miralda-Escudé J., Haehnelt M., Rees M. J., 2000, *ApJ*, 530, 1
- Muzahid S., Srianand R., Bergeron J., Petitjean P., 2012, *MNRAS*, 421, 446
- Nasir F., D'Aloisio A., 2019, *MNRAS*, preprint ([arXiv:1910.03570](https://arxiv.org/abs/1910.03570))
- Nasir F., Bolton J. S., Becker G. D., 2016, *MNRAS*, 463, 2335
- Nasir F., Bolton J. S., Viel M., Kim T.-S., Haehnelt M. G., Puchwein E., Sijacki D., 2017, *MNRAS*, 471, 1056
- Oppenheimer B. D., Davé R., 2009, *MNRAS*, 395, 1875
- Peebles M. S., Weinberg D. H., Davé R., Fardal M. A., Katz N., 2010, *MNRAS*, 404, 1281
- Penton S. V., Shull J. M., Stocke J. T., 2000, *ApJ*, 544, 150
- Planck Collaboration et al., 2014, *A&A*, 571, A16
- Planck Collaboration et al., 2018, preprint ([arXiv:1807.06209](https://arxiv.org/abs/1807.06209))
- Puchwein E., Bolton J. S., Haehnelt M. G., Madau P., Becker G. D., Haardt F., 2015, *MNRAS*, 450, 4081
- Puchwein E., Haardt F., Haehnelt M. G., Madau P., 2019, *MNRAS*, 485, 47
- Rauch M. et al., 1997, *ApJ*, 489, 7
- Rauch M., Sargent W. L. W., Womble D. S., Barlow T. A., 1996, *ApJ*, 467, L5
- Robertson B. E., Ellis R. S., Dunlop J. S., McLure R. J., Stark D. P., 2010, *Nature*, 468, 49
- Rollinde E., Theuns T., Schaye J., Pâris I., Petitjean P., 2013, *MNRAS*, 428, 540

- Rorai A. et al., 2017a, *Science*, 356, 418
 Rorai A. et al., 2017b, *MNRAS*, 466, 2690
 Rorai A., Carswell R. F., Haehnelt M. G., Becker G. D., Bolton J. S., Murphy M. T., 2018, *MNRAS*, 474, 2871
 Ross N. P., Cross N. J. G., 2019, *MNRAS*, 494, 789
 Rudie G. C., Steidel C. C., Pettini M., 2012, *ApJ*, 757, L30
 Schaye J., Theuns T., Leonard A., Efstathiou G., 1999, *MNRAS*, 310, 57
 Schaye J., Theuns T., Rauch M., Efstathiou G., Sargent W. L. W., 2000, *MNRAS*, 318, 817
 Shull J. M., Smith B. D., Danforth C. W., 2012, *ApJ*, 759, 23
 Springel V., 2005, *MNRAS*, 364, 1105
 Springel V., Hernquist L., 2002, *MNRAS*, 333, 649
 Storrie-Lombardi L. J., McMahon R. G., Irwin M. J., 1996, *MNRAS*, 283, L79
 Telikova K., Balashev S., Shternin P., 2018, preprint (arXiv e-prints)
 Telikova K. N., Shternin P. S., Balashev S. A., 2019, *ApJ*, 887, 205
 Theuns T., Schaye J., Haehnelt M. G., 2000, *MNRAS*, 315, 600
 Trac H., Cen R., Loeb A., 2008, *ApJ*, 689, L81
 Tripp T. M., Sembach K. R., Bowen D. V., Savage B. D., Jenkins E. B., Lehner N., Richter P., 2008, *ApJS*, 177, 39
 Viel M., Haehnelt M. G., Springel V., 2004a, *MNRAS*, 354, 684
 Viel M., Weller J., Haehnelt M. G., 2004b, *MNRAS*, 355, L23
 Viel M., Bolton J. S., Haehnelt M. G., 2009, *MNRAS*, 399, L39
 Viel M., Haehnelt M. G., Bolton J. S., Kim T.-S., Puchwein E., Nasir F., Wakker B. P., 2017, *MNRAS*, 467, L86
 Vogt S. S. et al., 1994, in Crawford D. L., Craine E. R., eds, Proc. SPIE Conf. Ser. Vol. 2198, Instrumentation in Astronomy VIII. SPIE, Bellingham, p. 362
 Walther M., Oñorbe J., Hennawi J. F., Lukić Z., 2019, *ApJ*, 872, 13
 Webb J. K., Carswell R. F., 1991, in Shaver P. A., Wampler E. J., Wolfe A. M., eds, Quasar Absorption Lines, p. 3
 Wu X., McQuinn M., Kannan R., D'Aloisio A., Bird S., Marinacci F., Davé R., Hernquist L., 2019, *MNRAS*, 490, 3177
 Wu X.-B. et al., 2015, *Nature*, 518, 512

SUPPORTING INFORMATION

Supplementary data are available at [MNRAS](https://www.mnras.org) online.

Figure A1. Examples of observed transmission spikes from the sample of 5 QSO sightlines.

Figure A2. The effect of continuum fitting uncertainty on the three statistics for simulated spectra: the spike width distribution (left panel), pCDDF (middle panel), and FPS (right panel) in *default* model.

Figure A3. Panel A shows the observed flux (F_{obs}) towards QSO PS0J239-07 (black curve).

Figure A4. The effect of continuum fitting uncertainty on the three statistics: the spike width distribution (left panel), pCDDF (middle panel), and FPS (right panel).

Figure A5. Calculation of sensitivity curve from observational sample in the three different redshift bins.

Figure B1. The effect of varying T_0 on spike statistics, showing the spike width distribution (left panel), pCDDF (middle panel), and FPS (right panel).

Figure B2. As for Fig. B1, except the effect of variation in γ on the spike statistics is illustrated.

Figure B3. As Fig. B1, except the effect of variation in Γ_{12} on the spike statistics is illustrated.

Figure B4. As for panel A in Fig. 9, except the recovery of T_0 and γ from *hot* and *cold* models is illustrated.

Figure B5. As for Fig. B1, except the effect of variation in the pressure smoothing scale on the spike statistics is illustrated.

Figure B6. As for panel A in Fig. 9, except the effect of variation in the pressure smoothing scale on the $T_0 - \gamma$ constraints is quantified in three redshift bins.

Figure C1. The effect of box size on the spike width distribution (left panel), pCDDF (middle panel), and FPS (right panel) in the Sherwood simulation suite at $z = 5.6$, for box sizes of $20h^{-1}$ cMpc (L20N512), $40h^{-1}$ cMpc (L40N1024), and $80h^{-1}$ cMpc (L80N2048) at fixed mass resolution, $m_{\text{gas}} \sim 7.97 \times 10^5 M_{\odot}$.

Figure C2. The effect of mass resolution on the spike width distribution (left panel), pCDDF (middle panel), and FPS (right panel) in the Sherwood simulation suite at $z = 5.6$, for a gas particle mass of $m_{\text{gas}} \sim 6.38 \times 10^6 M_{\odot}$ (L40N512), $m_{\text{gas}} \sim 7.97 \times 10^5 M_{\odot}$ (L40N1024), and $m_{\text{gas}} \sim 9.97 \times 10^4 M_{\odot}$ (L40N2048) for a fixed box size of $40h^{-1}$ cMpc.

Figure C3. The likelihood $\mathcal{L} = e^{-\chi^2/2}$ obtained by comparing the simulated spike width distribution to observations at $5.3 \leq z \leq 5.5$.

Table D1. Reduced χ^2 (i.e. χ^2 per degree of freedom) between model and observed statistics.

Please note: Oxford University Press is not responsible for the content or functionality of any supporting materials supplied by the authors. Any queries (other than missing material) should be directed to the corresponding author for the article.

This paper has been typeset from a \LaTeX file prepared by the author.